

Hydrogen and hydrogen-like-ion bound states and hyperfine splittings: finite nuclear size effects

Igor Kuzmenko^{1,2}, Tetyana Kuzmenko¹, Y. Avishai^{1,3}, Y. B. Band^{1,2,4}

¹*Department of Physics, Ben-Gurion University of the Negev, Beer-Sheva 84105, Israel*

²*Department of Chemistry, Ben-Gurion University of the Negev, Beer-Sheva 84105, Israel*

³*Yukawa Institute for Theoretical Physics, Kyoto, Japan*

⁴*The Ilse Katz Center for Nano-Science, Ben-Gurion University of the Negev, Beer-Sheva 84105, Israel*

Using the Dirac equation, we study corrections to electron binding energies and hyperfine splittings of atomic hydrogen and hydrogen-like ions due to finite nuclear size (FNS) effects, relativistic QED radiative corrections and nuclear recoil corrections. Three models for the charge distribution and the magnetic moment distribution within the nucleus are considered. Calculations are carried for light atoms (H, He and K) and heavy atoms (Rb, Cs, Pb, Bi, U). The FNS corrections to the ground-state energy are shown to be smaller than the electron-nucleus reduced mass corrections, and comparable to the relativistic QED radiative corrections for the light nuclei, but much larger than both these corrections for heavy nuclei. Comparison is made with an experiment on the $1s$ - $2s$ transition frequency for hydrogen. FNS corrections to the ground state hyperfine splitting are comparable in size to the relativistic QED radiative corrections for light nuclei, but are larger for heavy nuclei.

I. INTRODUCTION

Hydrogen is the most abundant element in the universe, and atomic hydrogen has the simplest electronic structure. If the proton in atomic hydrogen is taken as a point charge, analytic expressions for wave functions and bound-state energies exist within both the non-relativistic framework (using the Schrödinger equation) and the relativistic one (using the Dirac equation) [1–5]. This is also true for hydrogen-like ions (HLI) if the nucleus is taken as a point charge. Moreover, the ground state hyperfine splitting of these systems can also be obtained analytically (if the nuclear g -factor is known) [6–8]. However, nuclei are not point-like; even the proton is a composite particle with finite radius, $r_p = 0.8414(19) \times 10^{-15} \text{ m} = 1.5900(36) \times 10^{-5} \text{ Bohr}$ [9]. Here we consider the effects of a finite nuclear size (FNS) r_N (and the nuclear charge distribution), nuclear recoil corrections and QED radiative corrections on the electronic properties and hyperfine splittings of hydrogen and hydrogen-like ions (H&HLI).

Finite nuclear size (FNS) corrections (i.e., finite nuclear radius corrections) to the binding energies of H&HLI have been extensively studied, see e.g., Refs. [6–8, 10–17, 20–23] and references quoted therein. Theoretical investigations often use the Schrödinger equation with relativistic corrections, e.g., spin-orbit coupling, obtained using $1/c$ expansions [4]. One can apply Rayleigh–Schrödinger perturbation theory to calculate nuclear structure corrections for the ground state hyperfine splitting as well as the electronic transition energies [15]. However, the ground state binding energies, ϵ , of H&HLI with large nuclear charge, Ze , are not small compared to $m_e c^2$, where m_e is the electron mass, hence fully relativistic calculations are necessary. For example, for the uranium hydrogen-like ion, $\epsilon \approx 0.2588 m_e c^2$. Hence, using the Schrödinger equation (even with spin-

orbit interaction) is not satisfactory for heavy nuclei; one must use the Dirac equation. Moreover, even for light nuclei, one should use relativistic calculations to obtain high accuracy. In Ref. [15], the authors solve the Schrödinger equation and add relativistic corrections such as spin-orbit interaction. They assume that the nuclear charge is distributed homogeneously inside the nucleus and find the correction to the ground-state energy $(2/3)Z\epsilon_H r_N^2/a_0^2 \ll Z\epsilon_H$, where in Gaussian units $\epsilon_H = e^2/a_0$ is the Hartree energy, r_N is the nuclear charge radius, and a_0 is the Bohr radius. However, for high Z nuclei, the relativistic Dirac equation should be applied. In Refs. [16, 17], the authors solve the Dirac equation for hydrogen having a FNS with the charge distributed on the surface of the nucleus, approximate the position dependence of the wave function inside the nucleus by a polynomial, and find the binding energies for the ground and excited states. Note that perturbation theory for the FNS corrections using the Dirac equation is a good approximation for hydrogen and light nuclei. Such an approximation leads to a closed form expression for the FNS correction in the non-relativistic limit [see Eq. (69)]. However, perturbation theory is not valid for high Z nuclei.

H&HLI systems are traditionally used in ultra-high precision experimental tests of quantum mechanics, as well as of nuclear structure, since complications due to many-electron effects are absent [18, 19]. It will be crucial to compare the results of our calculations with these experiments. Furthermore, accurate experiments of muonic hydrogen atoms (muonic hydrogen contains a negatively charged muon instead of an electron) have been reported, see e.g., [8, 12].

Here, within a relativistic Dirac equation formulation, we calculate the FNS corrections to the ground ($1S_{1/2}$) and excited S states energies, and to the ground state hyperfine energy splittings, for a number of elements and their isotopes for H&HLI. We use three different models

for the spherically symmetric charge and magnetic moment distributions within the nucleus: In model (a) the nuclear charge and magnetic moment are distributed homogeneously on the surface of a sphere with radius r_a . In model (b) the charge and magnetic moment are distributed homogeneously inside the nucleus with radius r_b . In model (c) we use the so called two-parameter Fermi model (TPFM) for the nuclear charge density and magnetic moment density distributions [21, 22, 24], which fall off smoothly near the surface of nucleus. We use the same distribution for both nuclear charge and nuclear magnetic moment because of lack of parameters for the magnetic moment density.

We also calculate FNS corrections to the ground state hyperfine splitting of H&HLI due to (1) the correction for the charge distribution of the nucleus and (2) the correction for the magnetic moment distribution of the nucleus, i.e., the Bohr-Weisskopf correction [13, 14]. Measurements of the ground state hyperfine splitting of the H&HLI are among the most accurately measured quantities [6–8]. These measurements have been used to determine both nuclear radii and nuclear g -factors. To compare theoretical calculations for FNS corrections with experimental measurements, one needs to incorporate relativistic quantum electrodynamics (QED) radiative corrections [20]. FNS corrections to the ground-state hyperfine splitting have been analyzed in Refs. [6–8, 13, 14, 20–22, 26]. In Ref. [8], the authors report measurements of the hyperfine splitting of the ground state of hydrogen used to estimate the proton radius. In Refs. [7, 13, 14, 20, 21], the authors apply QED radiative corrections and calculate the FNS corrections to the ground-state hyperfine splitting of H&HLI. References [22, 26] studied the hyperfine splitting for high- Z HLI.

The paper is organized as follows. In Sec. II, we formulate the Dirac equation for the H&HLI with potential energy of the electron determined using models (a) and (b). Electron bound states for H&HLI are studied in Sec. III. The solution of the Dirac equation for a point-like nucleus is presented in Sec. III A. The analytic solution of the Dirac equation for model (a) is given in Sec III B and the numerical solution for model (b) is given in Sec III C. FNS effects on the ground-state energy for both models (a) and (b) are calculated in Sec. IV within perturbation theory. Section V discusses the TPFM for the nuclear charge distribution. Ground state hyperfine splittings are calculated in Sec. VI. Section VII estimates the uncertainty of the hyperfine splitting due to uncertainty in the nuclear g -factors, δg_I , and nuclear radii δr_N and Sec. VIII compares the results of models (a), (b) and (c) with experiments. In Sec. IX we summarize our main results. Several technical details are presented in the Appendices. Specifically, in Appendix A we discuss the root mean squared nuclear charge radius, r_N , in Appendix B we calculate the matrix elements of $\mathbf{e}_r \times \boldsymbol{\alpha}$, where \mathbf{e}_r is the basis vector in the direction of the position vector \mathbf{r} from the nucleus to the electron and $\boldsymbol{\alpha}$ is the vector of

the Dirac matrices. Appendix D discusses the magnetic moment distribution for nuclei with one nucleon outside a closed nuclear shell.

II. MODELS FOR FNS POTENTIALS

The stationary Dirac equation for H&HLI is given by,

$$\left[-i\hbar c \boldsymbol{\alpha} \cdot \nabla + V(r) + \beta m_e c^2 \right] \psi(\mathbf{r}) = \varepsilon \psi(\mathbf{r}), \quad (1)$$

where m_e is the electron mass, $\boldsymbol{\alpha}$ and β are the 4×4 Dirac matrices, and $V(r) = V_C(r) = -Ze^2/r$ is the Coulomb potential wherein Z is the nuclear charge. In model (a), the nuclear charge is distributed on the surface of the sphere of radius r_a and therefore the potential is constant within the nucleus, and in model (b) the nuclear charge density $\varrho_b(r)$ is uniformly distributed within a sphere of radius r_b ,

$$\varrho_b(r) = \frac{3Ze}{4\pi r_b^3} \Theta(r_b - r), \quad (2)$$

where $\Theta(\bullet)$ is the Heaviside theta function. Therefore the potential for model (b) is quadratic inside the nucleus. Explicit expressions for the potentials in models (a) and (b) are:

$$V_a(r) = \begin{cases} -\frac{Ze^2}{r_a}, & r \leq r_a, \\ -\frac{Ze^2}{r}, & r > r_a, \end{cases} \quad (3)$$

$$V_b(r) = \begin{cases} -\frac{Ze^2}{2r_b} \left(3 - \frac{r^2}{r_b^2} \right), & r \leq r_b, \\ -\frac{Ze^2}{r}, & r > r_b, \end{cases} \quad (4)$$

The nuclear radii r_a and r_b are expressed in terms of root mean square (RMS) nuclear charge radius r_N as [10, 27]:

$$r_a = r_N, \quad r_b = \sqrt{\frac{5}{3}} r_N. \quad (5)$$

See Appendix A for details.

The difference between the FNS potential and the Coulomb potential is the *repulsive* potential

$$W_\nu(r) = V_\nu(r) - V_C(r) \quad \nu = a, b. \quad (6)$$

Note that $V_\nu(r) = V_C(r) + W_\nu(r)$ is *less attractive* than $V_C(r)$ in both models. We also define the difference potential $W_{ba}(r) = V_b(r) - V_a(r)$,

$$W_{ba}(r) = \begin{cases} \frac{Ze^2}{r_a} - \frac{Ze^2}{2r_b} \left(3 - \frac{r^2}{r_b^2} \right), & r \leq r_a, \\ \frac{Ze^2}{r} - \frac{Ze^2}{2r_b} \left(3 - \frac{r^2}{r_b^2} \right), & r_a < r \leq r_b, \\ 0 & r > r_b, \end{cases} \quad (7)$$

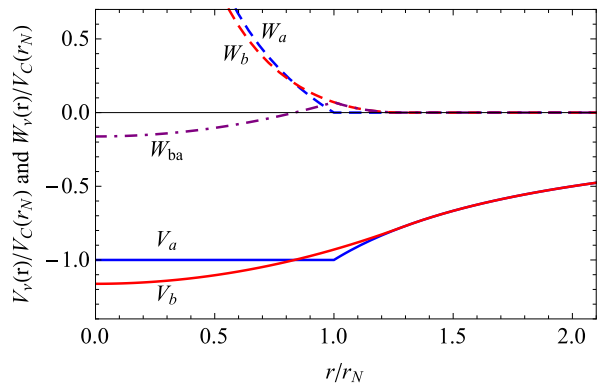


FIG. 1. The potentials $V_{\nu=a}(r)$ and $V_{\nu=b}(r)$ versus r for a hydrogen atom defined in Eqs. (3) and (4) (solid blue and red curves respectively). The repulsive potentials $W_{\nu}(r) = V_{\nu}(r) - V_C(r)$, (blue and red dashed curves respectively), and the difference potentials $W_{ab}(r)$ defined in Eq. (7) (dashed-dotted purple curve). Note that for $r > r_{\nu}$, $W_{\nu}(r) = 0$. Here r_a and r_b are given by Eq. (5).

which will be useful in our perturbation analysis below. $W_{ba}(r)$ needs to be added to $V_a(r)$ to get $V_b(r)$. Figure 1 plots the potentials $V_a(r)$ and $V_b(r)$ given in Eqs. (3) and (4), the repulsive potentials $W_{a,b}(r)$, and the difference potential $W_{ba}(r)$ versus r .

The nuclear radii r_a, r_b and their uncertainties $\delta r_a, \delta r_b$, are expressed in terms of the RMS nuclear charge radius r_N and its uncertainty δr_N as

$$\begin{aligned} r_a \pm \delta r_a &= r_N \pm \delta r_N, \\ r_b \pm \delta r_b &= \sqrt{\frac{5}{3}} (r_N \pm \delta r_N). \end{aligned} \quad (8)$$

The uncertainties δr_{ν} give rise to the uncertainties in $V_{\nu}(r)$:

$$V_{\nu}(r) \pm \delta V_{\nu}(r) = V_{\nu}(r) \pm \left| \frac{\partial V_{\nu}(r)}{\partial r_{\nu}} \right| \delta r_{\nu}. \quad (9)$$

Explicitly,

$$\delta V_a(r) = \frac{Ze^2 \delta r_a}{r_a^2} \Theta(r_a - r), \quad (10)$$

and

$$\delta V_b(r) = \frac{3Ze^2 \delta r_b}{2r_b^2} \left(1 - \frac{r^2}{r_b^2} \right) \Theta(r_b - r). \quad (11)$$

In Sec. V we will introduce the TPFM for the nuclear charge distribution [21, 22, 24], and we will refer to it as model (c) [see Eq. (80)]. In this model the nuclear charge distribution near r_N is smooth. Figure 2 plots the charge distribution for three different smoothing parameters and the charge distribution of model (b) (see the dashed curve). The shape of the TPFM charge distribution is sometimes called the Woods-Saxon shape. The potential of the TPFM charge distribution is also

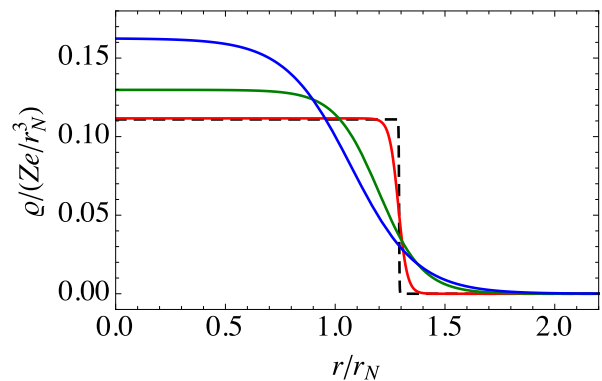


FIG. 2. The charge density ρ versus r/r_N for the TPFM [see Eq. (80)] for three different smoothing parameters (solid colored curves) and the model (b) charge density [see Eq. (2)] (dashed black curve). The integral of ρ over all space equals Ze .

referred to as the Woods-Saxon potential. It can be determined analytically and then numerical solution of the Dirac equation can be obtained.

The potential for this model can be determined analytically and then numerical solution of the Dirac equation eigenstates with this potential by numerically solving the Dirac equation for heavy nuclei.

III. DIRAC EQUATION BOUND STATES

The Dirac 4-component spinor wave function $\psi(\mathbf{r})$ can be written in the form [29],

$$\psi(\mathbf{r}) = \begin{pmatrix} g(r) \Omega_{jlm} \\ if(r) \Omega_{jl'm} \end{pmatrix}, \quad (12)$$

where Ω_{jlm} is a normalized spherical harmonic spinor which is an eigenfunction of the total electronic angular momentum operator squared, \mathbf{J}^2 , the electronic orbital angular momentum operator squared, \mathbf{L}^2 , the electronic spin angular momentum operator squared, \mathbf{S}^2 and the z -projection of the total electronic angular momentum operator, J_z . These have eigenvalues $j(j+1)$, $l(l+1)$, $\frac{3}{4}$ and m , where $l = j \pm \frac{1}{2}$ and $l' = 2j - l$. The radial wave functions $g(r)$ and $f(r)$ satisfy the equations,

$$\begin{aligned} \hbar c \left[(rg(r))' + \frac{\kappa}{r} (rg(r)) \right] &= \\ [m_e c^2 - V(r) + \varepsilon] (rf(r)), & \end{aligned} \quad (13a)$$

$$\begin{aligned} \hbar c \left[(rf(r))' - \frac{\kappa}{r} (rf(r)) \right] &= \\ [m_e c^2 + V(r) - \varepsilon] (rg(r)), & \end{aligned} \quad (13b)$$

where $\kappa = -1$ for the s -state. **S or s ?**

A. Solution of the Dirac equation (13) for the point-like nucleus

The solution of Eqs. (13) for the point-like nucleus (i.e., for $r_N = 0$) is well known [29]; for an s -state,

$$g(r) = \mathcal{N} \sqrt{m_e c^2 + \varepsilon} \left[Q_1(\rho) + Q_2(\rho) \right] \rho^{\gamma-1} e^{-\rho/2}, \quad (14a)$$

$$f(r) = -\mathcal{N} \sqrt{m_e c^2 - \varepsilon} \left[Q_1(\rho) - Q_2(\rho) \right] \rho^{\gamma-1} e^{-\rho/2}, \quad (14b)$$

where \mathcal{N} is a normalization constant found from the equation, $\int_0^\infty (|g(r)|^2 + |f(r)|^2) r^2 dr = 1$. Here we define the quantities

$$\rho = \frac{2\lambda r}{\hbar c}, \quad \lambda = \sqrt{m_e^2 c^4 - \varepsilon^2}, \quad \gamma = \sqrt{\kappa^2 - Z^2 \alpha^2}, \quad (15)$$

and $\alpha = \frac{e^2}{\hbar c}$ is the fine structure constant (where the right hand side of the equation is given in Gaussian units). The functions $Q_1(\rho)$ and $Q_2(\rho)$ are [29]

$$Q_1(\rho) = A_1 F\left(\gamma - \frac{Z\alpha\varepsilon}{\lambda}, 2\gamma + 1, \rho\right), \quad (16a)$$

$$Q_2(\rho) = A_2 F\left(\gamma + 1 - \frac{Z\alpha\varepsilon}{\lambda}, 2\gamma + 1, \rho\right), \quad (16b)$$

where $F(a, b, \rho)$ is the Kummer confluent hypergeometric function. The normalization constants A_1 and A_2 are related as follows:

$$A_2 = -\frac{\gamma\lambda - Z\alpha\varepsilon}{\kappa\lambda - Z\alpha m_e c^2} A_1. \quad (17)$$

In the special case,

$$\gamma - \frac{Z\alpha\varepsilon}{\lambda} = -n_r, \quad (18)$$

where n_r is a positive integer, the Kummer function reduces to a Laguerre polynomial,

$$F(-n_r, 2\gamma + 1, \rho) = \frac{\Gamma(2\gamma + 1)\Gamma(n_r + 1)}{\Gamma(2\gamma + n_r + 1)} L_{n_r}^{(2\gamma)}(\rho),$$

why there is no number?

and thus, the functions $g(r)$ and $f(r)$ in Eq. (14) decay exponentially for $r \rightarrow \infty$. In the special case,

$$\gamma - \frac{Z\alpha\varepsilon}{\lambda} = 0, \quad \text{and} \quad \kappa < 0,$$

$A_2 = 0$ and $Q_1(\rho)$ decay exponentially for $r \rightarrow \infty$. Otherwise, when

$$\gamma - \frac{Z\alpha\varepsilon}{\lambda} \neq -n_r,$$

$Q_1(\rho)$ and $Q_2(\rho)$ diverge as e^ρ when $\rho \rightarrow \infty$, and thus $g(r)$ and $f(r)$ in Eq. (14) diverge as $e^{\rho/2}$.

Let us recall the expressions for the relativistic energies $\varepsilon_n^{(0)}$ of a H&HLI system calculated for a point-like nucleus [29],

$$\varepsilon_n^{(0)} = m_e c^2 + \hbar c R_\infty \frac{2\mathcal{G}(n)}{1 + \mu_{ep}}, \quad (19)$$

where, for arbitrary Z , $\mu_{ep} \equiv m_e/M(Z, A)$ is the electron to nuclear mass ratio, $M(Z, A)$ is the mass of the nucleus comprising Z protons and $A - Z$ neutrons, and cR_∞ is the Rydberg frequency, which is related to the Hartree energy ε_H , $cR_\infty = \frac{\varepsilon_H}{2\hbar} [= \frac{e^4 m_e}{4\pi\hbar^3}$ in Gaussian units]. In Eq. (19) $n = 1, 2, 3, \dots$ is the principal quantum number, and

$$\begin{aligned} \mathcal{G}(n) &= \frac{1}{Z^2 \alpha^2} \left[\frac{1}{\sqrt{1 + X_n^2}} - 1 \right] \\ &= -\frac{1}{Z^2 \alpha^2} \frac{X_n^2}{\sqrt{1 + X_n^2} [\sqrt{1 + X_n^2} + 1]}, \end{aligned} \quad (20)$$

where $X_n = \frac{Z\alpha}{\sqrt{1 - Z^2 \alpha^2 + n - 1}}$. We found that the first form on the right-hand side of Eq. (20) can lead to significant numerical errors, so for numerical calculations, the second form is preferable. As noted in Refs. [30–33], the concept of a reduced mass in the Dirac equation is ambiguous to some extent. Nevertheless, the necessity of introducing the reduced mass as the substitution for electron mass *in the Dirac energy and the Dirac equation* in order to obtain theoretical results that are close to experimental results has been stressed in the literature (see Refs. [30–33]). The ground state energy in Eq. (19) ($n = 1$) is

$$\varepsilon_1^{(0)}(Z, A) = m_e c^2 + m c^2 (\sqrt{1 - Z^2 \alpha^2} - 1), \quad (21)$$

where $m \equiv m(Z, A)$ is the electron-nucleus reduced mass,

$$m \equiv m(Z, A) = \frac{m_e}{1 + \mu_{ep}}, \quad (22)$$

and the ground-state wave functions in Eq. (14) are,

$$g(r) = \frac{2Z^{3/2} \sqrt{1 + \gamma}}{a_B^{3/2} \sqrt{\Gamma(2\gamma + 1)}} \rho^{\gamma-1} e^{-\rho/2}, \quad (23a)$$

$$f(r) = -\frac{2Z^{3/2} \sqrt{1 - \gamma}}{a_B^{3/2} \sqrt{\Gamma(2\gamma + 1)}} \rho^{\gamma-1} e^{-\rho/2}, \quad (23b)$$

where a_B is taken to be the *effective* Bohr radius, including the reduced mass effect, and is given (in Gaussian units) by

$$a_B = \frac{\hbar^2}{m e^2}. \quad (24)$$

The nuclear radii r_N are tabulated in Table I for a number of nuclei.

The energies $\varepsilon_1^{(0)}$ and $\varepsilon_2^{(0)}$ in Eq. (19) are plotted in Fig. 3 as functions of Z . For $Z\alpha < 1$, $\varepsilon_1^{(0)}$ and $\varepsilon_2^{(0)}$ satisfy the inequalities,

$$0 < \varepsilon_1^{(0)} < \varepsilon_2^{(0)} < m_e c^2.$$

TABLE I. RMS nuclear charge radii r_N and their uncertainties δr_N (in Bohr radius units a_B). Data for the proton and deuteron are taken from Ref. [10], and data for the other isotopes are taken from Ref. [27]. Here (and below) E^{-n} is shorthand notation for $\times 10^{-n}$.

Isotope (Z, A)	r_N	δr_N
H(1, 1)	$1.5900E^{-5}$	$3.6E^{-8}$
H(1, 2)	$4.02132E^{-5}$	$1.40E^{-8}$
H(1, 3)	$3.3242E^{-5}$	$6.86E^{-7}$
He(2, 3)	$3.7154E^{-5}$	$5.7E^{-8}$
He(2, 4)	$3.1662E^{-5}$	$5.3E^{-8}$
K(19, 39)	$6.4910E^{-5}$	$3.6E^{-8}$
K(19, 40)	$6.4971E^{-5}$	$5.3E^{-8}$
K(19, 41)	$6.5230E^{-5}$	$1.04E^{-7}$
Rb(37, 85)	$7.9437E^{-5}$	$4.5E^{-8}$
Rb(37, 87)	$7.9348E^{-5}$	$3.4E^{-8}$
Cs(55, 133)	$9.0784E^{-5}$	$8.7E^{-8}$
Cs(55, 135)	$9.0833E^{-5}$	$8.9E^{-8}$
Pb(82, 204)	$1.03563E^{-4}$	$2.6E^{-8}$
Pb(82, 206)	$1.03750E^{-4}$	$2.6E^{-8}$
Pb(82, 207)	$1.03827E^{-4}$	$2.6E^{-8}$
Pb(82, 208)	$1.03958E^{-4}$	$2.5E^{-8}$
Bi(83, 209)	$1.04334E^{-4}$	$4.9E^{-8}$
U(92, 235)	$1.10241E^{-4}$	$7.7E^{-8}$
U(92, 236)	$1.10419E^{-4}$	$7.2E^{-8}$
U(92, 238)	$1.10683E^{-4}$	$6.2E^{-8}$

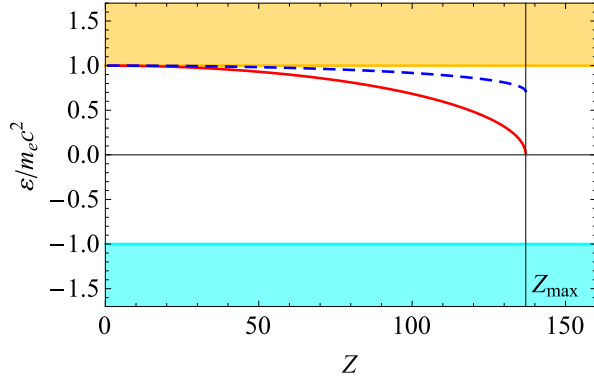


FIG. 3. Energies of the 1s bound state $\varepsilon_1^{(0)}$ (solid red curve) and the excited 2s state $\varepsilon_2^{(0)}$ (dashed blue curve) for the H&HLI isotopes defined in Eq. (19) as functions of the proton number Z . The gold and turquoise regions show the continuous energy spectrum with $|\varepsilon| > m_e c^2$. The horizontal line is $\varepsilon = 0$, and the vertical line indicates $Z_{\max} = 137$.

For $Z = Z_{\max} = 137$, $\varepsilon_1^{(0)} = 0.02292 m_e c^2$ and $\varepsilon_2^{(0)} = 0.71516 m_e c^2$. For $Z > Z_{\max}$, the parameter γ in Eq. (15) becomes imaginary, and the wave function in Eq. (23) is singular as $r \rightarrow 0$ [29]. Indeed, the Dirac equation (13) with the Coulomb potential of a point-like nucleus is meaningful only for $Z < 137$.

B. Dirac equation (13) solution for Model (a)

Equations (13) for model (a) potential are solved separately for $r > r_N$ and for $r < r_N$, to obtain the corresponding wave functions $f_{\pm}(r)$ and $g_{\pm}(r)$ up to as yet unknown multiplicative constants A_{\pm} . The matching conditions at $r = r_N$ are,

$$A_- g_-(r_N) = A_+ g_+(r_N), \quad A_- f_-(r_N) = A_+ f_+(r_N). \quad (25)$$

The set of equations (25) has nontrivial solutions when the determinant

$$\mathfrak{D}(\varepsilon) \equiv g_-(r_N) f_+(r_N) - g_+(r_N) f_-(r_N) = 0. \quad (26)$$

Note that the condition above is necessary but not sufficient to assure that $g_- = g_+$ and $f_- = f_+$ at r_N .

1. Solution of Dirac equation (13) for $r > r_N$

The solution of Eqs. (13) can be written in the form [29]

$$f_+(r) = \sqrt{\frac{m_e c^2 - \varepsilon}{m_e c^2}} \left[Q_1(\rho) + Q_2(\rho) \right] \rho^{\gamma-1} e^{-\rho/2}, \quad (27a)$$

$$g_+(r) = \sqrt{\frac{m_e c^2 + \varepsilon}{m_e c^2}} \left[Q_2(\rho) - Q_1(\rho) \right] \rho^{\gamma-1} e^{-\rho/2}, \quad (27b)$$

where ρ , λ and γ are given by Eq. (15). The functions $Q_1(\rho)$ and $Q_2(\rho)$ satisfy the equations,

$$\begin{aligned} \rho Q_1'(\rho) + \left(\gamma - \frac{Z\alpha\varepsilon}{\lambda} \right) Q_1(\rho) \\ - \left(\kappa - \frac{Z\alpha m_e c^2}{\lambda} \right) Q_2(\rho) = 0, \end{aligned} \quad (28a)$$

$$\begin{aligned} \rho Q_2'(\rho) + \left(\gamma + \frac{Z\alpha\varepsilon}{\lambda} - \rho \right) Q_2(\rho) \\ - \left(\kappa + \frac{Z\alpha m_e c^2}{\lambda} \right) Q_1(\rho) = 0, \end{aligned} \quad (28b)$$

where the prime denotes differentiation with respect to ρ , and $\kappa = -1$ for the s states. **S or s ?** Substituting $\kappa = -1$ into Eq. (28a), we can express $Q_2(\rho)$ in terms of $Q_1(\rho)$ and $Q_1'(\rho)$ as follows,

$$\begin{aligned} Q_2(\rho) = -\frac{\lambda}{\lambda + Z\alpha m_e c^2} \left[\rho Q_1'(\rho) \right. \\ \left. + \left(\gamma - \frac{Z\alpha\varepsilon}{\lambda} \right) Q_1(\rho) \right]. \end{aligned} \quad (29)$$

Substituting this equation into Eq. (28b), we find

$$\rho Q_1''(\rho) + (2\gamma + 1 - \rho) Q_1'(\rho) - \left(\gamma - \frac{Z\alpha\varepsilon}{\lambda} \right) Q_1(\rho) = 0. \quad (30)$$

The solution of Eq. (30) that vanishes at $\rho \rightarrow \infty$ is [29]

$$Q_1(\rho) = AU\left(\gamma - \frac{Z\alpha\varepsilon}{\lambda}, 2\gamma + 1, \rho\right), \quad (31)$$

where $U(a, b, \rho)$ is the confluent hypergeometric function.

Similarly, substituting in Eq. (28b) $\kappa = -1$, we can express $Q_1(\rho)$ in terms of $Q_2(\rho)$ and $Q'_2(\rho)$,

$$Q_1(\rho) = -\frac{\lambda}{\lambda - Z\alpha m_e c^2} \left[\rho Q'_2(\rho) + \left(\gamma + \frac{Z\alpha\varepsilon}{\lambda} - \rho\right) Q_2(\rho) \right]. \quad (32)$$

Substituting Eq. (32) into Eq. (28a), we get

$$\rho Q_2''(\rho) + (2\gamma + 1 - \rho) Q_2'(\rho) - \left(\gamma + 1 - \frac{Z\alpha\varepsilon}{\lambda}\right) Q_2(\rho) = 0. \quad (33)$$

Solution of Eq. (33) vanishing at $\rho \rightarrow \infty$ is [29]

$$Q_2(\rho) = BU\left(\gamma + 1 - \frac{Z\alpha\varepsilon}{\lambda}, 2\gamma + 1, \rho\right). \quad (34)$$

Substituting Eqs. (31) and (34) into Eq. (29), we get

$$A = \frac{\lambda}{m_e c^2}, \quad B = \frac{\lambda - Z\alpha m_e c^2}{m_e c^2}. \quad (35)$$

Alternatively, we can substitute Eqs. (31) and (34) into Eq. (32), and get Eq. (35). Finally, the solution of the Dirac equation (13) for $r > r_N$ is,

$$f_+(r) = \sqrt{\frac{m_e c^2 - \varepsilon}{m_e c^2}} \rho^{\gamma-1} e^{-\rho/2} \times \left[\frac{\lambda}{m_e c^2} U\left(\gamma - \frac{Z\alpha\varepsilon}{\lambda}, 2\gamma + 1, \rho\right) + \frac{\lambda - Z\alpha m_e c^2}{m_e c^2} U\left(\gamma + 1 - \frac{Z\alpha\varepsilon}{\lambda}, 2\gamma + 1, \rho\right) \right], \quad (36a)$$

$$g_+(r) = -\sqrt{\frac{m_e c^2 + \varepsilon}{m_e c^2}} \rho^{\gamma-1} e^{-\rho/2} \times \left[\frac{\lambda}{m_e c^2} U\left(\gamma - \frac{Z\alpha\varepsilon}{\lambda}, 2\gamma + 1, \rho\right) - \frac{\lambda - Z\alpha m_e c^2}{m_e c^2} U\left(\gamma + 1 - \frac{Z\alpha\varepsilon}{\lambda}, 2\gamma + 1, \rho\right) \right]. \quad (36b)$$

2. Dirac equation (13) solution for $r < r_N$

An analytic solution for the case of constant potential inside the nucleus is well-known [2]. Equation (13a) allows us to express $(rf_-(r))$ in terms of $(rg_-(r))$ and $(rg_-(r))'$,

$$(rf_-(r)) = \frac{\hbar c}{m_e c^2 - V(r_N) + \varepsilon} \times \left[(rg_-(r))' - \frac{1}{r} (rg_-(r)) \right]. \quad (37)$$

Substituting Eq. (37) into Eq. (13b), we get

$$(rg_-(r))'' + k^2(\varepsilon)(rg_-(r)) = 0, \quad (38)$$

where

$$k(\varepsilon) = \frac{1}{\hbar c} \sqrt{(\varepsilon - V(r_N))^2 - m_e^2 c^4}. \quad (39)$$

The nonsingular solution of Eq. (38) at $r = 0$ is,

$$g_-(r) = C \frac{\sin(k(\varepsilon)r)}{k(\varepsilon)r}, \quad (40)$$

where C is a normalization constant.

Equation (13b) allows us to express $(rg_-(r))$ in terms of $(rf_-(r))$ and $(rf_-(r))'$,

$$(rg_-(r)) = \frac{\hbar c}{m_e c^2 + V(r_N) - \varepsilon} \times \left[(rf_-(r))' + \frac{1}{r} (rf_-(r)) \right]. \quad (41)$$

Substituting Eq. (41) into Eq. (13a), we get

$$(rf_-(r))'' + \left(k^2(\varepsilon) - \frac{2}{r^2}\right) (rf_-(r)) = 0. \quad (42)$$

The nonsingular solution of Eq. (42) at $r = 0$ is,

$$f_-(r) = D \frac{k(\varepsilon)r \cos(k(\varepsilon)r) - \sin(k(\varepsilon)r)}{k^2(\varepsilon)r^2}, \quad (43)$$

where D is a normalization constant.

Substituting Eqs. (40) and (43) into Eq. (37), we get

$$\frac{D}{C} = \sqrt{\frac{\varepsilon - V(r_N) - m_e c^2}{\varepsilon - V(r_N) + m_e c^2}}. \quad (44)$$

Alternatively, we can substitute Eqs. (40) and (43) into Eq. (41), and get Eq. (44). Finally, the solution of the Dirac equation (13) for $r < r_N$ is,

$$f_-(r) = \sqrt{\frac{\varepsilon - V(r_N) - m_e c^2}{m_e c^2}} \times \frac{k(\varepsilon)r \cos(k(\varepsilon)r) - \sin(k(\varepsilon)r)}{k^2(\varepsilon)r^2}, \quad (45a)$$

$$g_-(r) = \sqrt{\frac{\varepsilon - V(r_N) + m_e c^2}{m_e c^2}} \frac{\sin(k(\varepsilon)r)}{k(\varepsilon)r}. \quad (45b)$$

n	1	2	3
ϵ_n	0.499734640577	0.1249340759790	0.0555260711867
$\epsilon_n^{(0)}$	0.499734640745	0.1249340760015	0.0555260711927

TABLE II. Hydrogen binding energies $\epsilon_n(r_N)$ in Hartree calculated for model (a) using Eq. (26), and the hydrogen atom Dirac energies $\epsilon_n^{(0)}$ for $r_N = 0$ (i.e., for point-like proton) in Eq. (19). r_N is given in Table I.

3. Boundary conditions at $r = r_N$

The functions $f_{\pm}(r)$ and $g_{\pm}(r)$ satisfy the boundary conditions specified in Eq. (26) at $r = r_N$. Clearly, $f_{\pm}(r_N)$ and $g_{\pm}(r_N)$ in Eqs. (36) and (45), and hence \mathfrak{D} in Eq. (26) depend on ϵ . Solving the equation $\mathfrak{D}(\epsilon) = 0$ for ϵ yields the energies of the hydrogen atom. These are tabulated in Table II. Figure 4(a) plots the function

$$\tilde{\mathfrak{D}}(\epsilon) = \mathfrak{L}(\epsilon)\mathfrak{D}(\epsilon), \quad (46)$$

versus ϵ for $Z = 1$, $r_N = 0.8414 \times 10^{-13}$ cm (the proton RMS radius [10]) and $|\epsilon| < 0.9 m_e c^2$, where $\mathfrak{D}(\epsilon)$ is given in Eq. (26), and

$$\mathfrak{L}(\epsilon) = \frac{m_e^2 c^4 - \epsilon^2}{m_e^2 c^4}.$$

$\mathfrak{L}(\epsilon)$ is positive for $|\epsilon| < m_e c^2$. Both $\tilde{\mathfrak{D}}(\epsilon)$ and $\mathfrak{L}(\epsilon)$ are dimensionless. The wave functions in Eqs. (36) and (45) are dimensionless and will be normalized in what follows [by multiplying by the factor \mathcal{N}_n given by Eq. (47), where the dimensions of \mathcal{N}_n is $[\mathcal{N}_n] = \text{Length}^{-3/2}$]. $\tilde{\mathfrak{D}}(\epsilon)$ is positive, and there are no bound states in the interval $-m_e c^2 < \epsilon < 0.99 m_e c^2$. Figure 4(b) shows $\tilde{\mathfrak{D}}(\epsilon)$ for ϵ close to and below $m_e c^2$. $\tilde{\mathfrak{D}}(\epsilon) = 0$ when ϵ is very close to the Dirac energies $\epsilon_n^{(0)}$ of the hydrogen atom given by Eq. (19) with $Z = A = 1$, where the subscript (0) indicates the point charge nucleus limit.

The binding energies $\epsilon_n(r_N)$ (with $n = 1, 2, 3$ and r_N being the nuclear radius of ${}^1\text{H}$) calculated numerically from Eq. (26) and $\epsilon_n^{(0)} = m_e c^2 - \epsilon_n^{(0)}$, with $\epsilon_n^{(0)}$ given in Eq. (19), are listed in Table II. It is seen that $|\epsilon_1(r_N) - \epsilon_1^{(0)}| \approx 1.680 \times 10^{-10}$ Hartree, which is clearly very much smaller than $\epsilon_1^{(0)}$. The Dirac energies $\epsilon_n(r_N)$ are pushed up by the repulsive potential $W_a(r) = [V_C(r_N) - V_C(r)]\Theta(r_N - r)$ [see Eq. (6)]. Note the following inequalities:

$$|\epsilon_{n+1}(r_N) - \epsilon_{n+1}^{(0)}| \ll |\epsilon_n(r_N) - \epsilon_n^{(0)}|,$$

where $n = 1, 2, 3, \dots$

4. Wave functions

We now consider normalization of the wave functions g_n and f_n . Here $g_n(r)$ is given by Eqs. (36b) for $r >$

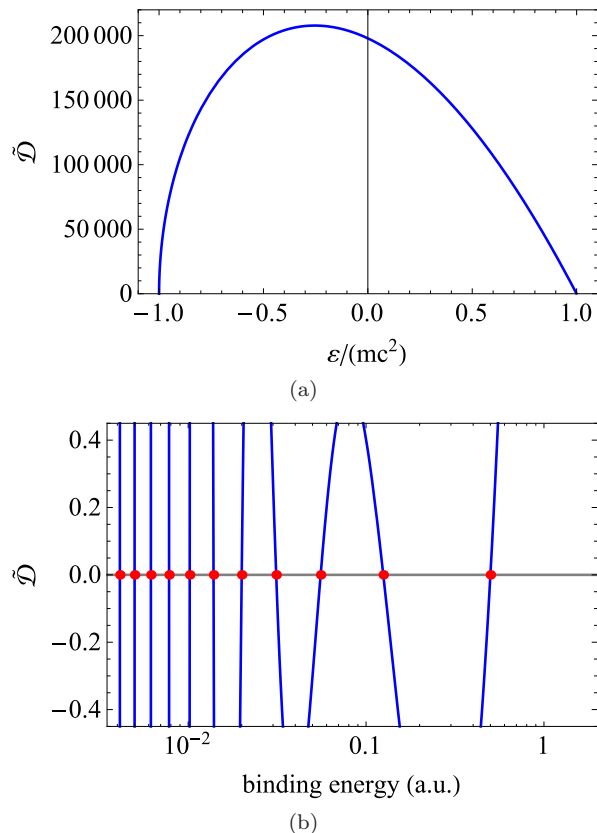


FIG. 4. (a) The function $\tilde{\mathfrak{D}}(\epsilon)$ defined in Eq. (46) versus the energy ϵ for $|\epsilon| < 0.999 m_e c^2$. (b) Log-linear plot of $\tilde{\mathfrak{D}}(\epsilon)$ in Eq. (46) as a function of the binding energy $\epsilon = m_e c^2 - \epsilon$ (blue curve) for ϵ close to $m_e c^2$ (the range includes the 11 lowest s ${}^1\text{H}$ states). The red dots show the Dirac binding energies $\epsilon_n^{(0)}$ of the hydrogen atom with zero proton radius (i.e., the Dirac energies). Here $\tilde{\mathfrak{D}}(\epsilon)$ is dimensionless, and the binding energy in (b) is in Hartree.

r_N and by Eq. (45b) for $r < r_N$, and $f_n(r)$ is given by Eq. (36a) for $r > r_N$ and by Eq. (45a) for $r < r_N$. The normalization constants \mathcal{N}_n are chosen such that

$$\mathcal{N}_n^2 \int_0^\infty [g_n^2(r) + f_n^2(r)] r^2 dr = 1. \quad (47)$$

Figure 5 plots $\mathcal{N}_1(g_1(r), f_1(r))$ for the $1s$ state. The functions $(g_1(r), f_1(r))$ and their derivatives $(g_1'(r), f_1'(r))$ are continuous at $r = r_N$, where $r_N = 1.658 \times 10^{-5} a_B$. $g_1(r)$ has no nodes, has a maximum at $r = 0$, and vanishes as $r \rightarrow \infty$. $f_1(r)$ vanishes at $r = 0$ and is negative for finite r ; it reaches its minimum and tends to zero as $r \rightarrow \infty$.

Figure 6 is a log-linear plot for the $2s$ normalized wave function $\mathcal{N}_2(g_2(r), f_2(r))$. The functions $(g_2(r), f_2(r))$ and their derivatives $(g_2'(r), f_2'(r))$ are continuous at $r = r_N$. $g_2(r)$ has a maximum at $r = 0$, and one node. It vanishes at $r \gg a_B$. $f_2(r)$ has two nodes: one node at $r = 0$, and another node at finite r ; it vanishes as $r \rightarrow \infty$.

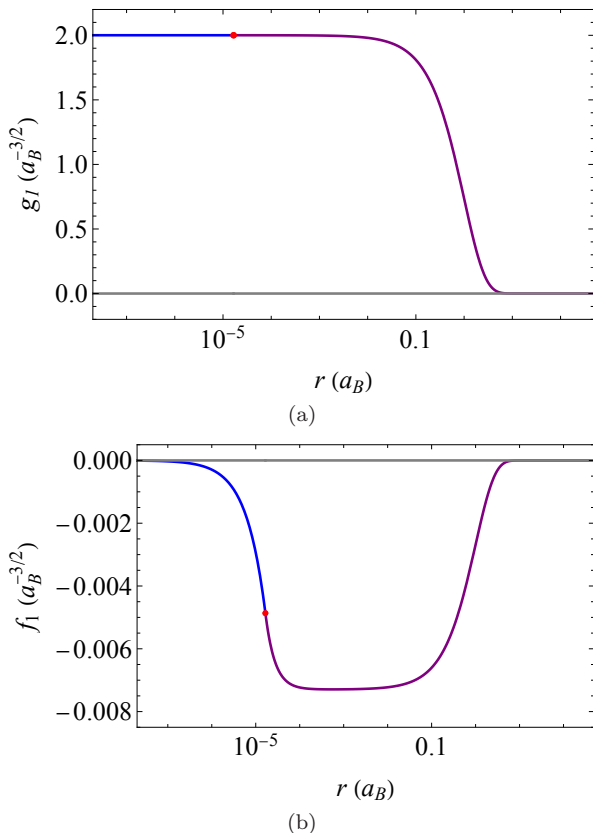


FIG. 5. Log-linear plot of (a) $\mathcal{N}g_1(r)$ and (b) $\mathcal{N}f_1(r)$ for the $1s$ state of hydrogen atom with the energy ε_1 (in Hartree). Here $g_1(r)$ is given by Eq. (36b) for $r > r_N$ (purple) and by Eq. (45b) for $r < r_N$ (blue). $f_1(r)$ is given by Eq. (36a) for $r > r_N$ (purple) and by Eq. (45a) for $r < r_N$ (blue). The normalization constant \mathcal{N} is found from Eq. (47). The red dots show $g_1(r_N)$ and $f_1(r_N)$.

5. $1s$ and $2s$ state energies for various isotopes

We now solve the determinantal equation (26) for model (a) (constant potential inside the nucleus) and find the FNS corrections to the energies of the ground $1s$ state and the first excited $2s$ state for various isotopes.

Tables III and IV show the FNS corrections

$$\varepsilon_{n,a} = \varepsilon_n - \varepsilon_n^{(0)}, \quad n = 1, 2. \quad (48)$$

Here ε_1 and ε_2 are calculated numerically using Eq. (26), and $\varepsilon_1^{(0)}$ and $\varepsilon_2^{(0)}$ are given in analytic form by Eq. (19). $\varepsilon_{1,a}$ and $\varepsilon_{2,a}$ are functions of the nuclear radius $r_a = r_N$, where r_N is tabulated in Table I. The uncertainty in r_N gives rise to uncertainty $\delta\varepsilon_{n,a}$ in $\varepsilon_{n,a}$, which can be estimated as,

$$\delta\varepsilon_{n,a} = \left| \frac{\partial\varepsilon_{n,a}}{\partial r_N} \right| \delta r_N. \quad (49)$$

The FNS correction $\varepsilon_{1,a}$ to the ground-state energy, and the uncertainty $\delta\varepsilon_{1,a}$ are tabulated in Table III, and the FNS correction $\varepsilon_{2,a}$ to the excited-state energy, and the

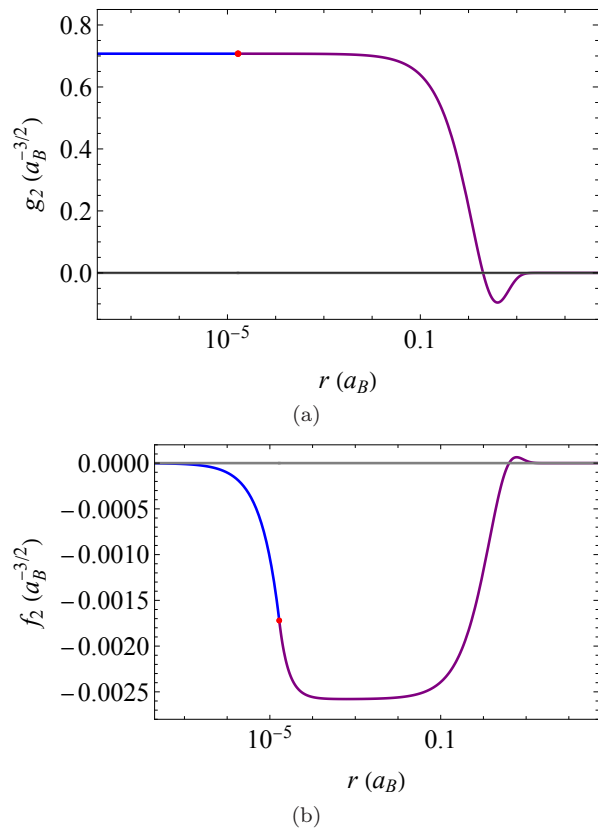


FIG. 6. The log-linear plot of (a) $\mathcal{N}_2g_2(r)$ and (b) $\mathcal{N}_2f_2(r)$ for the $2s$ state of hydrogen atom with the energy ε_2 (in Hartree). Here $g_2(r)$ is given by Eq. (36b) for $r > r_N$ (purple) and by Eq. (45b) for $r < r_N$ (blue). $f_2(r)$ is given by Eq. (36a) for $r > r_N$ (purple) and by Eq. (45a) for $r < r_N$ (blue). The normalization constant \mathcal{N}_2 is found from Eq. (47). The red dots show the wave functions at $r = r_N$.

uncertainty $\delta\varepsilon_{2,a}$ are tabulated in Table IV. The corrections $\varepsilon_{1,a}$ and $\varepsilon_{2,a}$ satisfy the inequalities $\varepsilon_{1,a} \gg \varepsilon_{2,a} > 0$. Note that, for isotopes of atoms with a given Z , $\varepsilon_{1,a}$ and $\varepsilon_{2,a}$ do not always increase with A . This is because the nuclear radii r_N in Table I for some isotopes are not monotonic with A (see r_N for He and Rb). The repulsive potential $W_a(r)$ in Eq. (6) increases with the nuclear radius r_N , and r_N increases with Z , see Table I, hence the energy correction ε_a in Table III increases with Z .

Table IV shows the calculated FNS corrections $\varepsilon_{2,a}$ and $\varepsilon_{2,b}$. The FNS corrections to the $1s$ - $2s$ hydrogen transition frequency $\Delta\omega_{1s,2s}^{(a)}$ and $\Delta\omega_{1s,2s}^{(b)}$ are defined as,

$$\Delta\omega_{1s,2s}^{(a)} = \frac{1}{\hbar} (\varepsilon_{2,a} - \varepsilon_{1,a}), \quad \Delta\omega_{1s,2s}^{(b)} = \frac{1}{\hbar} (\varepsilon_{2,b} - \varepsilon_{1,b}). \quad (50)$$

Note that the method to accurately measure the isotope shifts of atomic transitions reported in Ref. [38] can be used to experimentally probe the isotope shifts calculated here.

Equation (19) for a point-like nucleus and the numerical calculations with the nuclear charge distribution for models (a) and (b) take into account recoil effects by

TABLE III. FNS corrections $\varepsilon_{1,a}$ and $\varepsilon_{1,b}$ (in Hartree) to the energy of the ground $1s$ state of H&HLI. The numbers in the brackets indicate the uncertainties $\delta\varepsilon_{1,a}$ and $\delta\varepsilon_{1,b}$ in the calculated ground-state energy due to the uncertainty in the nuclear radius r_N in Table I [see Eqs. (49) and (59)]. The concise notation used for errors is explained in Ref. [34].

Isotope (Z, A)	$\varepsilon_{1,a}(\delta\varepsilon_{1,a})$	$\varepsilon_{1,b}(\delta\varepsilon_{1,b})$
H(1, 1)	$1.6837(76)E^{-10}$	$1.6837(76)E^{-10}$
H(1, 2)	$1.07773(75)E^{-9}$	$1.07773(75)E^{-9}$
H(1, 3)	$7.37(30)E^{-10}$	$7.37(30)E^{-10}$
He(2, 3)	$1.4746(45)E^{-8}$	$1.4746(45)E^{-8}$
He(2, 4)	$1.0711(36)E^{-8}$	$1.0711(36)E^{-8}$
K(19, 39)	$4.1987(46)E^{-4}$	$4.1974(46)E^{-4}$
K(19, 40)	$4.2064(68)E^{-4}$	$4.2051(68)E^{-4}$
K(19, 41)	$4.240(13)E^{-4}$	$4.238(13)E^{-4}$
Rb(37, 85)	$1.2547(14)E^{-2}$	$1.2534(14)E^{-2}$
Rb(37, 87)	$1.2520(12)E^{-2}$	$12507(12)E^{-2}$
Cs(55, 133)	0.13135(23)	0.13107(23)
Cs(55, 135)	0.13148(23)	0.13120(23)
Pb(82, 204)	2.4687(10)	2.4586(10)
Pb(82, 206)	2.4758(10)	2.4657(10)
Pb(82, 207)	2.4787(10)	2.4686(10)
Pb(82, 208)	2.48367(93)	2.47351(93)
Bi(83, 209)	2.7559(20)	2.7444(20)
U(92, 235)	7.3062(75)	7.2718(75)
U(92, 236)	7.3234(69)	7.2889(69)
U(92, 238)	7.3490(60)	7.3143(60)

TABLE IV. FNS corrections $\varepsilon_{2,a}$ and $\varepsilon_{2,b}$ (in Hartree) to the energy of the excited $2s$ state of H&HLI. The numbers in brackets indicate the uncertainties $\delta\varepsilon_{2,a}$ and $\delta\varepsilon_{2,b}$ in the calculated ground-state energy due to the uncertainty in the nuclear radius r_N given in Table I [see Eqs. (49) and (59)].

Isotope (Z, A)	$\varepsilon_{2,a}(\delta\varepsilon_{2,a})$	$\varepsilon_{2,b}(\delta\varepsilon_{2,b})$
H(1, 1)	$2.1047(95)E^{-11}$	$2.1047(95)E^{-11}$
H(1, 2)	$1.34722(94)E^{-10}$	$1.34722(94)E^{-10}$
H(1, 3)	$9.21(38)E^{-11}$	$9.21(38)E^{-11}$
He(2, 3)	$1.8436(56)E^{-9}$	$1.8436(56)E^{-9}$
He(2, 4)	$1.3391(45)E^{-9}$	$1.3391(45)E^{-9}$
K(19, 39)	$5.3381(58)E^{-5}$	$5.3365(58)E^{-5}$
K(19, 40)	$5.3480(86)E^{-5}$	$5.3463(86)E^{-5}$
K(19, 41)	$5.390(17)E^{-5}$	$5389(17)E^{-5}$
Rb(37, 85)	$1.6732(18)E^{-3}$	$1.6714(18)E^{-3}$
Rb(37, 87)	$1.6696(16)E^{-3}$	$1.6678(16)E^{-3}$
Cs(55, 133)	$1.8969(33)E^{-2}$	$1.8928(33)E^{-2}$
Cs(55, 135)	$1.8988(34)E^{-2}$	$1.8947(34)E^{-2}$
Pb(82, 204)	0.42868(17)	0.42692(17)
Pb(82, 206)	0.42991(17)	0.42814(17)
Pb(82, 207)	0.43041(17)	0.42864(17)
Pb(82, 208)	0.43127(16)	0.42950(16)
Bi(83, 209)	0.48259(36)	0.48057(36)
U(92, 235)	1.3880(14)	1.3814(14)
U(92, 236)	1.3912(13)	1.3846(13)
U(92, 238)	1.3961(11)	1.3895(11)

replacing the electron mass m_e by the reduced mass $m \equiv m(Z, A)$ defined in Eq. (22). This naive expression can be used as a starting point for calculating the recoil corrections to the electron energy levels. An explicit expression for the s -state energies with the reduced mass dependence is derived from quantum electrodynamics in Ref. [33],

$$\varepsilon_n^{(\text{Dirac})} = m_e c^2 + Z^2 hcR_\infty \times \left[\frac{2\mathcal{G}(n)}{1 + \mu_{ep}} - \frac{\mu_{ep} Z^2 \alpha^2 \mathcal{G}^2(n)}{(1 + \mu_{ep})^3} \right]. \quad (51)$$

The dimensionless function $\mathcal{G}(n)$ is given in Eq. (20). The first two terms on the right hand side of Eq. (51) give the energy of the s state in Eq. (19), but the last term in this equation, which is proportional to $\mathcal{G}^2(n)$ is proportional to $\mu_{ep}(Z\alpha)^4$. This term vanishes in the limit of infinitely large nuclear mass, and hence is absent in Eq. (19). For hydrogen, this correction term to the energy is

$$hcR_\infty \frac{\mu_e \alpha^2 \mathcal{G}^2(n)}{(1 + \mu_{ep})^3} \approx \frac{7.2 \times 10^{-9}}{n^2} \epsilon_H.$$

The Dirac energy in Eq. (51) can be expanded in a power series in $Z^2\alpha^2$, as in Eq. (3.4) of Ref. [33]:

$$\tilde{\varepsilon}_n^{(\text{Dirac})} = m_e c^2 - \frac{hcR_\infty}{1 + \mu_{ep}} \left\{ \frac{Z^2}{n^2} + \frac{Z^4 \alpha^2}{n^3} \left(1 - \frac{3}{4n} + \frac{\mu_{ep}}{(1 + \mu_{ep})^2} \frac{1}{4n} \right) \right\}. \quad (52)$$

Equation (52) is a power series expansion of Eq. (51) in α^2 , up to α^4 (recall that a factor of α^2 is contained in R_∞). The $1s$ energy obtained using (52) differs from that obtained using (51) by about a MHz.

C. Dirac equation (13) solutions for model (b)

Here we find the wave functions and binding energies of H&HLI with nuclear charge distributed homogeneously inside a sphere of radius r_b defined in Eq. (5). The potential $V_b(r)$ in Eq. (4) is harmonic inside the nucleus. In this case an analytic solution is unknown. We rewrite Eq. (13) with $\kappa = -1$ as,

$$\frac{\hbar c r^2 g'_-(r)}{m c^2 - V_b(r) + \varepsilon} = r^2 f_{b,-}(r), \quad (53a)$$

$$(r^2 f_{b,-}(r))' = \frac{m c^2 + V_b(r) - \varepsilon}{\hbar c} r^2 g_{b,-}(r). \quad (53b)$$

Differentiating Eq. (53a) and using Eq. (53b) we get the following second-order differential equation for $g_{b,-}(r)$:

$$\frac{1}{r^2} \frac{d}{dr} \left(\frac{r^2}{m c^2 - V_b(r) + \varepsilon} \frac{d g_{b,-}(r)}{dr} \right) = \frac{1}{\hbar^2 c^2} [m c^2 + V_b(r) - \varepsilon] g_{b,-}(r). \quad (54)$$

We solve Eq. (54) numerically and find the radial wave function $g_{b,-}(r)$ for $r < r_b$. For this purpose, we need the binding energy of the atom (which we do not know). In order to find the energy and the wave function, we apply the iteration method described below. The radial wave function $f_{b,-}(r)$ can be found from the equation,

$$f_{b,-}(r) = \frac{\hbar c g'_{b,-}(r)}{m c^2 - V_b(r) + \varepsilon}. \quad (55)$$

The ground-state wave functions satisfy the boundary conditions at $r = 0$,

$$f_{b,-}(0) = 0, \quad g_{b,-}(0) = 1. \quad (56)$$

The radial wave functions $g_+(r)$ and $f_+(r)$ with $r > r_b$ are given in Eq. (36), and the radial wave functions $g_b(r), f_b(r)$ satisfy the boundary conditions at $r = r_b$,

$$A_- g_{b,-}(r_b) = A_+ g_+(r_b), \quad A_- f_{b,-}(r_b) = A_+ f_+(r_b). \quad (57)$$

Here A_{\pm} are (unknown) normalization constants. The set of equations (57) has nontrivial solutions when the determinant $\mathfrak{D}(\varepsilon)$ vanishes, where

$$\mathfrak{D}(\varepsilon) = g_{b,-}(r_b) f_+(r_b) - g_+(r_b) f_{b,-}(r_b). \quad (58)$$

Appendix C explains the iteration method for finding the ground state and excited s state energies using Eq. (58).

The uncertainty $\delta\varepsilon_{n,b}$ in the model (b) energy $\varepsilon_{n,b}$ of the ns state is estimated as,

$$\delta\varepsilon_{n,b} = \int_0^{r_b} \delta V_b(r) \left[|g_{n,-}(r)|^2 + |f_{n,-}(r)|^2 \right] r^2 dr, \quad (59)$$

where $\delta V_b(r)$ is given in Eq. (11), and $n = 1$ for the ground state.

The FNS correction $\varepsilon_{1,b}$ to the ground-state energy, and the uncertainty $\delta\varepsilon_{1,b}$ are tabulated in Table III, and the FNS correction $\varepsilon_{2,b}$ to the excited-state energy, and the uncertainty $\delta\varepsilon_{2,b}$ are tabulated in Table IV. Note that for light isotopes, i.e., for H, He and K, $\varepsilon_{n,a}$ and $\varepsilon_{n,b}$ [$n = 1, 2$] and their uncertainties $\delta\varepsilon_{n,a}$ and $\delta\varepsilon_{n,b}$ satisfy the relations

$$\delta\varepsilon_{n,a} \approx \delta\varepsilon_{n,b} > \varepsilon_{n,a} - \varepsilon_{n,b},$$

whereas for the heavy isotopes,

$$\delta\varepsilon_{n,a} \approx \delta\varepsilon_{n,b} < \varepsilon_{n,a} - \varepsilon_{n,b}.$$

Therefore, the comparison of the calculated and measured ground-state binding energies of heavy HLI (such as Rb, Cs, Pb, Bi and U) can be used to determine the nuclear charge distribution. The ground-state energy of the hydrogen atom, and of light HLI (such as He and K) are almost the same for models (a) and (b), hence, measuring the ground-state binding energies would not be an accurate method for determining the nuclear charge distributions.

The numerical solution technique developed in this subsection can be generalized to the case of other charge distributions inside the nucleus, e.g., for the TPFM charge distribution [21, 22] introduced in Eq. (80) below.

We calculated the FNS corrections analytically for model (a) and numerically for model (b). The results were tabulated in Table III for the ground $1s$ state of H&HLI, and in Table IV for the first excited $2s$ state. For comparison, we will calculate in Sec. IV below the FNS correction using perturbation theory. We shall show that the perturbation theory is a good approximation for the FNS corrections for H and light HLI, compare Tables VII and III. For heavy HLI, the perturbation theory results in Table VII are dissimilar to the results in Table III, i.e., the perturbation theory is poor. References [10] and [11] (2018 CODATA and 2002 CODATA) and many other papers use perturbation theory to calculate FNS corrections for hydrogen and light HLIs. These references expand the FNS corrections in a power series in r_N . In contrast, we numerically calculate the perturbation theory.

D. Finite-nuclear size corrections in 2018 CODATA

Finite-nuclear-size and nuclear-polarizability corrections are ordered by powers in α , following Ref. [10]:

$$\varepsilon_n^{(2018)} = \sum_{i=4}^{\infty} \varepsilon_n^{(i)}, \quad (60)$$

where n is the principal quantum number, and index i indicates the power of $Z\alpha$ in the expansion. The first and lowest-order contributions to s -state energies are

$$\varepsilon_n^{(4)} = \frac{2}{3} m_e c^2 \frac{(Z\alpha)^4}{n^3} \left(\frac{m}{m_e} \right)^3 \left(\frac{r_N}{\lambda_C} \right)^2, \quad (61)$$

where $\lambda_C = \hbar/(m_e c)$ is the reduced Compton wavelength. The numerical value of λ_C is given in Ref. [10] as, $\lambda_C = 3.8615926796(12) \times 10^{-12}$ m. Equation (61) is a non-relativistic approximation to the FNS correction to the s -state energy of H&HLI. Reference [10] gives relativistic corrections $\varepsilon_n^{(i)}$ with $i \geq 5$ just for hydrogen and deuterium atoms, but not for tritium atoms or for hydrogen-like ions.

For H&HLIs the FNS correction $\varepsilon_n^{(4)}$ to the ns -state energy and its uncertainty $\delta\varepsilon_n^{(4)}$ due to the uncertainty of the nuclear RMS charge radius are tabulated in Table V for the ground $n = 1$ state, and in Table VI for the first excited $n = 2$ state. These tables also show $\Delta\varepsilon_{n,a}^{(4)}$ and $\Delta\varepsilon_{n,b}^{(4)}$ where

$$\Delta\varepsilon_{n,\nu}^{(4)} = \varepsilon_n^{(4)} - \varepsilon_{n,\nu}, \quad (62)$$

and $\nu = a, b$ for the models (a) and (b) of the nuclear charge distribution. We will now compare $\varepsilon_1^{(4)} \approx \varepsilon_1^{(2018)}$ with $\varepsilon_{1,a}$ and $\varepsilon_{1,b}$ in Table III, and $\varepsilon_2^{(4)} \approx \varepsilon_2^{(2018)}$ with

TABLE V. FNS corrections $\varepsilon_1^{(4)}$ (in Hartree) to the energy of the ground $1s$ state of H&HLI. The numbers in the brackets indicate the uncertainties $\delta\varepsilon_1^{(4)}$ in the calculated ground-state energy due to the uncertainty in the nuclear radius r_N in Table I. $\Delta\varepsilon_{1,\nu}$ with $\nu = a, b$ is given in Eq. (62).

Isotope (Z, A)	$\varepsilon_1^{(4)}(\delta\varepsilon_1^{(4)})$	$\Delta\varepsilon_{1,a}^{(4)}$	$\Delta\varepsilon_{1,b}^{(4)}$
H(1, 1)	1.6827(76) E^{-10}	10 E^{-13}	10 E^{-13}
H(1, 2)	1.07719(75) E^{-9}	5.4 E^{-13}	5.4 E^{-13}
H(1, 3)	7.36(30) E^{-10}	4 E^{-13}	4 E^{-13}
He(2, 3)	1.4716(45) E^{-8}	3.0 E^{-11}	3.0 E^{-11}
He(2, 4)	1.0689(36) E^{-8}	2.2 E^{-11}	2.2 E^{-11}
K(19, 39)	3.6604(40) E^{-4}	5.383 E^{-5}	5.370 E^{-5}
K(19, 40)	36673(60) E^{-4}	5.392 E^{-5}	5.379 E^{-5}
K(19, 41)	3.697(12) E^{-4}	5.43 E^{-5}	5.42 E^{-5}
Rb(37, 85)	7.884(9) E^{-3}	4.663 E^{-3}	4.650 E^{-3}
Rb(37, 87)	7.866(8) E^{-3}	4.653 E^{-3}	4.640 E^{-3}
Cs(55, 133)	5.028(10) E^{-2}	8.108 E^{-2}	8.079 E^{-2}
Cs(55, 135)	5.033(10) E^{-2}	8.115 E^{-2}	8.087 E^{-2}
Pb(82, 204)	0.32327(17)	2.1455	2.1354
Pb(82, 206)	0.32444(17)	2.1514	2.1412
Pb(82, 207)	0.32493(17)	2.1538	2.1437
Pb(82, 208)	0.32574(16)	2.15793	2.14777
Bi(83, 209)	0.34440(32)	2.4115	2.4000
U(92, 235)	0.58042(82)	6.7258	6.6913
U(92, 236)	0.58229(76)	6.7411	6.7066
U(92, 238)	0.58509(66)	6.7639	6.7293

$\varepsilon_{2,a}$ and $\varepsilon_{2,b}$ in Table IV for H&HLIs. Moreover, for hydrogen and light HLIs, we compare $\Delta\varepsilon_{n,\nu}^{(4)}$ with the uncertainty $\delta\varepsilon_{n,\nu}$ of the FNS correction in Table III and IV. For ^AH atoms and He ions, $\Delta\varepsilon_{n,\nu}^{(4)} < \delta\varepsilon_{n,\nu}$, and therefore the non-relativistic approximation in Eq. (61) is a good approximation to the FNS correction to the $1s$ state energy ($n = 1$) and to the $2s$ state energy ($n = 2$). For heavier HLI, $\Delta\varepsilon_{n,\nu}^{(4)} > \delta\varepsilon_{n,\nu}$, and the non-relativistic approximation fails.

IV. PERTURBATION THEORY CORRECTIONS DUE TO FNS

In this section we apply perturbation theory for models (a) and (b) and find the corrections to the ground-state energies of H&HLI (assuming the potentials $W_\nu(r)$ and $W_{ba}(r)$ are small).

To be specific, we will concentrate on the ground electronic state, $n = 1$, and therefore the subscript n on energies and wave functions will often be omitted below. Since an analytic solution to the Dirac equation for a harmonic potential is not known, we use perturbation theory in order to obtain FNS corrections for model (b), but we also numerically solve the Dirac equation (see previous section).

Perturbation theory for models (a) and (b) with weak $W_\nu(r)$ is detailed in Sec. IV A. It starts from the Hamil-

TABLE VI. FNS corrections $\varepsilon_2^{(4)}$ (in Hartree) to the energy of the first excited $2s$ state of H&HLI. The numbers in the brackets indicate the uncertainties $\delta\varepsilon_2^{(4)}$ in the calculated ground-state energy due to the uncertainty in the nuclear radius r_N in Table I. $\Delta\varepsilon_{2,\nu}$ with $\nu = a, b$ is given in Eq. (62).

Isotope (Z, A)	$\varepsilon_2^{(4)}(\delta\varepsilon_2^{(4)})$	$\Delta\varepsilon_{2,a}^{(4)}$	$\Delta\varepsilon_{2,b}^{(4)}$
H(1, 1)	2.1034(75) E^{-11}	1.3 E^{-14}	1.3 E^{-14}
H(1, 2)	1.34648(94) E^{-10}	7.4 E^{-14}	7.4 E^{-14}
H(1, 3)	9.20(38) E^{-11}	5 E^{-14}	5 E^{-14}
He(2, 3)	1.8396(56) E^{-9}	4.1 E^{-12}	4.1 E^{-12}
He(2, 4)	1.3361(45) E^{-9}	3.0 E^{-12}	3.0 E^{-12}
K(19, 39)	4.5755(51) E^{-5}	7.626 E^{-6}	7.610 E^{-6}
K(19, 40)	4.5841(75) E^{-5}	7.639 E^{-6}	7.623 E^{-6}
K(19, 41)	4.621(15) E^{-5}	7.70 E^{-6}	7.68 E^{-6}
Rb(37, 85)	9.855(11) E^{-4}	6.877 E^{-4}	6.859 E^{-4}
Rb(37, 87)	9.833(10) E^{-4}	6.863 E^{-4}	6.846 E^{-4}
Cs(55, 133)	6.285(12) E^{-3}	1.2684 E^{-2}	1.2643 E^{-2}
Cs(55, 135)	6.292(12) E^{-3}	1.2696 E^{-2}	1.2655 E^{-2}
Pb(82, 204)	4.0409(21) E^{-2}	0.38827	0.38651
Pb(82, 206)	4.0555(21) E^{-2}	0.38935	0.38758
Pb(82, 207)	4.0616(21) E^{-2}	0.38980	0.38803
Pb(82, 208)	4.0718(19) E^{-2}	0.39055	0.38878
Bi(83, 209)	4.3050(41) E^{-2}	0.43954	0.43752
U(92, 235)	7.255(10) E^{-2}	1.3154	1.3088
U(92, 236)	7.2787(95) E^{-2}	1.3184	1.3118
U(92, 238)	7.3136(82) E^{-2}	1.3229	1.3163

tonian, $H_\nu = -i\hbar c\boldsymbol{\alpha} \cdot \nabla + V_\nu(r) + \beta mc^2$, rewritten as,

$$H_\nu = H_0 + V_\nu(r) - V_C(r) \equiv H_0 + W_\nu(r), \quad (63)$$

where $H_0 = -i\hbar c\boldsymbol{\alpha} \cdot \nabla + V_C(r) + \beta mc^2$ is the Dirac Hamiltonian for a point-like nucleus with $V_C(r) = -Ze^2/r$.

Perturbation theory for model (b) alone with weak $W_{ba}(r)$ is detailed in Sec. IV B. It starts from the Hamiltonian H_b in the form,

$$H_b = H_a + W_{ba}(r), \quad (64)$$

where H_a is given in Eq. (63), and $W_{ba}(r) = V_b(r) - V_a(r)$ is given in Eq. (7).

A. Perturbation theory with $W_\nu(r)$

The first-order correction to the energy is,

$$\varepsilon_{n,\nu}^{(1)} = \mathcal{N}^2 \int_0^{r_\nu} W_\nu(r) [g^2(r) + f^2(r)] r^2 dr, \quad (65)$$

where $f(r)$ and $g(r)$ are defined in Eq. (23). Note that the singularities at $r = 0$ of $f(r)$ and $g(r)$ are integrable

[29] and $W_\nu(r)$ is given by Eq. (6). Explicitly,

$$\begin{aligned} \varepsilon_{n,\nu}^{(1)} = & \frac{\hbar^3 c^3 \mathcal{N}^2}{8\lambda^3} \int_0^{\rho_\nu} W_\nu \left(\frac{\hbar c \rho}{2\lambda} \right) \left\{ m_e c^2 [Q_1^2(\rho) + Q_2^2(\rho)] \right. \\ & \left. + 2\varepsilon Q_1(\rho)Q_2(\rho) \right\} \rho^{2\gamma} e^{-\rho} d\rho, \end{aligned} \quad (66)$$

where

$$\begin{aligned} \mathcal{N}^{-2} = & \frac{\hbar^3 c^3}{8\lambda^3} \int_0^\infty \left\{ m_e c^2 [Q_1^2(\rho) + Q_2^2(\rho)] \right. \\ & \left. + 2\varepsilon Q_1(\rho)Q_2(\rho) \right\} \rho^{2\gamma} e^{-\rho} d\rho, \end{aligned} \quad (67)$$

and the dimensionless nuclear radius is

$$\rho_\nu = \frac{2\lambda r_\nu}{\hbar c} = \frac{2Zr_\nu}{a_B}. \quad (68)$$

Equation (15) was used to obtain the second equality in Eq. (68). The nuclear radii r_N are tabulated in Table I for a number of elements and isotopes. Let us restore the n dependence in $\varepsilon_{n,\nu}^{(1)}$. The FNS corrections $\varepsilon_{1,\nu}^{(1)}$ to the ground-state energy are given in Table VII. The dependence of $\varepsilon_{1,\nu}^{(1)}$ on A and Z follows the behavior of the nuclear radius $r_N(A, Z)$; because r_N increases with Z , so does $\varepsilon_{1,\nu}^{(1)}$. Dependence of $\varepsilon_{1,\nu}^{(1)}$ on A is less simple. For most of the elements in Table I, r_N increases with A , and so does $\varepsilon_{1,\nu}^{(1)}$, [see, e.g., $\varepsilon_{1,a}^{(1)}$ and $\varepsilon_{1,b}^{(1)}$ for isotopes of K, Cs, Pb and U]. However, for some elements, r_N decreases with A , and so does $\varepsilon_{1,\nu}^{(1)}$, [see, e.g., $\varepsilon_{1,a}^{(1)}$ and $\varepsilon_{1,b}^{(1)}$ for isotopes of He and Rb]. Moreover, for some elements, r_N is not a monotonic function of A , hence $\varepsilon_{1,\nu}^{(1)}$ is also not a monotonic function of A . For example, the nuclear radii $r_N(^A\text{H})$ for the isotopes ^AH satisfy the inequalities,

$$r_N(^1\text{H}) < r_N(^3\text{H}) < r_N(^2\text{H}).$$

Thus $\varepsilon_{1,\nu}^{(1)}(^A\text{H})$ satisfy

$$\varepsilon_{1,\nu}^{(1)}(^1\text{H}) < \varepsilon_{1,\nu}^{(1)}(^3\text{H}) < \varepsilon_{1,\nu}^{(1)}(^2\text{H}).$$

Comparing $\varepsilon_{1,a}^{(1)}$ in Table VII with ε_a in Table III shows that for light isotopes, perturbation theory predictions are very close to the non-perturbative numerical calculations, but for the heavy isotopes, the differences between $\varepsilon_{1,a}$ and $\varepsilon_{1,a}^{(1)}$ are large (see the difference between the values of $\varepsilon_{1,a}$ in Table III and $\varepsilon_{1,a}^{(1)}$ in Table VII).

In the non-relativistic approximation, the perturbation theory of the FNS correction, $\varepsilon_{n,\nu}^{(1)}$, takes the form of the simple equation [10, 11]

$$\varepsilon_{n,\nu}^{(1)} \approx \frac{2m_e c^2}{3} \frac{(Z\alpha)^4}{n^3} \frac{m^3}{m_e^3} \frac{r_N^2}{\lambda_C^2}. \quad (69)$$

We verified that this is an excellent approximation for hydrogen. The perturbation theory result in Eq. (69)

TABLE VII. First-order perturbation theory correction due to FNS in Eq. (66), for $\varepsilon_{1,\nu}^{(1)}$ [with $\nu = a, b$]. The nuclear radii r_a and r_b are given in Eq. (5), and the RMS nuclear charge radii r_N are listed in Table I.

Isotope (Z, A)	$\varepsilon_{1,a}^{(1)}$ (Hartree)	$\varepsilon_{1,b}^{(1)}$ (Hartree)
H (1, 1)	1.683743E ⁻¹⁰	1.683736E ⁻¹⁰
H (1, 2)	1.077785E ⁻⁹	1.077778E ⁻⁹
H (1, 3)	7.36714E ⁻¹⁰	7.36710E ⁻¹⁰
He (2, 3)	1.47484E ⁻⁸	1.47482E ⁻⁸
He (2, 4)	1.07128E ⁻⁸	1.07126E ⁻⁸
K (19, 39)	4.24722E ⁻⁴	4.24232E ⁻⁴
K (19, 40)	4.25506E ⁻⁴	4.25015E ⁻⁴
K (19, 41)	4.28869E ⁻⁴	4.28374E ⁻⁴
Rb (37, 85)	1.31164E ⁻²	1.30612E ⁻²
Rb (37, 87)	1.30882E ⁻²	1.30331E ⁻²
Cs (55, 133)	0.145819	0.144503
Cs (55, 135)	0.145964	0.144646
Pb (82, 204)	3.25838	3.19659
Pb (82, 206)	3.26777	3.20580
Pb (82, 207)	3.27167	3.20962
Pb (82, 208)	3.27822	3.21605
Bi(83, 209)	3.67177	3.60062
U (92, 235)	10.7543	10.5056
U (92, 236)	10.7799	10.5305
U (92, 238)	10.8180	10.5677

is obtained from Eq. (66) by using the approximations: $Q_1(\rho) \approx Q_1(0)$, $Q_2(\rho) \approx Q_2(0)$ and $\gamma \approx 1$. The first and second approximations are based on the inequalities $0 < \rho < \rho_\nu \ll 1$ [see Eq. (66)] which are valid for H and all HLIs. The third approximation is based on the inequality $Z\alpha \ll 1$ which is satisfied for H and light HLIs. For the heavy HLIs, $Z\alpha$ is not a small parameter, and Eq. (69) should be modified. The FNS correction to the ground state energy of all HLIs is

$$\varepsilon_{1,a}^{(1)} \approx \frac{2m_e c^2}{\gamma(2\gamma+1)} \frac{(Z\alpha)^4}{n^3} \frac{m^3}{m_e^3} \frac{r_N^{2\gamma}}{\lambda_C^{2\gamma}}, \quad (70a)$$

$$\varepsilon_{1,b}^{(1)} \approx \frac{5\gamma 3^{1-\gamma} 2m_e c^2}{\gamma(2\gamma+1)(2\gamma+3)} \frac{(Z\alpha)^4}{n^3} \frac{m^3}{m_e^3} \frac{r_N^{2\gamma}}{\lambda_C^{2\gamma}}. \quad (70b)$$

Note that the FNS correction to the $1s$ state energy of H and light HLIs in Eq. (69) depends just on the nuclear RMS charge radius r_N , and not on the details of the nuclear charge distribution. However, for heavy HLIs with high Z , the FNS correction to the s state energy is sensitive to the details of the nuclear charge distribution, and Eqs. (70a) and (70b) give different FNS corrections for the models (a) and (b). Therefore, it is important to develop and use more accurate models for the nuclear charge distribution in order to obtain better comparisons with the experimental energies of the s state and the frequencies of the $1s$ - $2s$ and $1s$ - $3s$ transitions.

B. Perturbation theory with $W_{ba}(r)$

The first order correction $\varepsilon_{ba}^{(1)}$ is given by,

$$\varepsilon_{ba}^{(1)} = \frac{4\pi A_-^2}{\mathcal{N}_a} \int_0^{r_a} W_{ba}(r) [g_-^2(r) + f_-^2(r)] r^2 dr + \frac{4\pi A_+^2}{\mathcal{N}_a} \int_{r_a}^{r_b} W_{ba}(r) [g_+^2(r) + f_+^2(r)] r^2 dr, \quad (71)$$

where $g_{\pm}(r)$ and $f_{\pm}(r)$ are the radial wave functions for the model (a). The functions $g_+(r)$ and $f_+(r)$ are given in Eq. (36), and $g_-(r)$ and $f_-(r)$ are given in Eq. (45). The constants A_{\pm} are found from Eq. (25), and the normalization constant \mathcal{N}_a is,

$$\mathcal{N}_a = 4\pi A_-^2 \int_0^{r_a} [g_-^2(r) + f_-^2(r)] r^2 dr + 4\pi A_+^2 \int_{r_a}^{\infty} [g_+^2(r) + f_+^2(r)] r^2 dr. \quad (72)$$

In order to calculate $\varepsilon_{ba}^{(1)}$, it is useful to rewrite Eq. (71) employing the electron density $\varrho_a(r)$ given by,

$$\varrho_a(r) = \begin{cases} \frac{4\pi A_-^2}{\mathcal{N}} [g_-^2(r) + f_-^2(r)], & r < r_a, \\ \frac{4\pi A_+^2}{\mathcal{N}} [g_+^2(r) + f_+^2(r)], & r > r_a, \end{cases} \quad (73)$$

hence Eq. (71) can be written as

$$\varepsilon_{ba}^{(1)} = \int_0^{r_b} W_{ba}(r) \varrho_a(r) r^2 dr. \quad (74)$$

The two-component wave function in Eq. (12) is continuous at $r = r_a$, i.e.,

$$A_- (g_-(r_a), f_-(r_a)) = A_+ (g_+(r_a), f_+(r_a)),$$

and thus the electron density $\varrho_a(r)$ in Eq. (73) is also continuous. Moreover, $\varrho_a(r)$ is smooth within the interval $0 < r < r_b$, i.e., for any $r \in (0, r_b)$, the following inequality is satisfied: $|\varrho(r) - \varrho(r_a)| \ll \varrho(r_a)$. Note that, although one may expect that Eq. (74) can be approximated as

$$\varepsilon_{ba}^{(1)} \approx \varrho(r_a) \int_0^{r_b} W_{ba}(r) r^2 dr, \quad (75)$$

it can be easily verified that $\int_0^{r_b} W_{ba}(r) r^2 dr = 0$, hence the approximation in Eq. (75) is not valid.

TABLE VIII. Perturbation theory corrections $\varepsilon_{ba}^{(1)}$ [in Hartree] to the ground state of H&HLI systems [see Eq. (76)]. The dimensionless parameter δ_{ba} is defined in Eq. (77). The energy correction $\varepsilon_{1,ba}$ and its uncertainty $\delta\varepsilon_{1,ba}$ due to the uncertainty in the nuclear RMS nuclear charge radius [in units of Hartree] are calculated non-perturbatively from Eqs. (78) and (79).

Isotope (Z, A)	$\varepsilon_{ba}^{(1)}$	δ_{ba}	$\varepsilon_{1,ba} (\delta\varepsilon_{1,ba})$
H (1, 1)	$-2.39058E^{-16}$	$-4.78371E^{-16}$	$-3.26(15)E^{-16}$
H (1, 2)	$-2.37631E^{-15}$	$-4.75385E^{-15}$	$-2.48(3)E^{-15}$
H (1, 3)	$-1.91704E^{-15}$	$-3.83472E^{-15}$	$-1.57(11)E^{-15}$
He (2, 3)	$-8.14903E^{-14}$	$-4.07504E^{-14}$	$-8.59(4)E^{-14}$
He (2, 4)	$-5.4718E^{-14}$	$-2.73613E^{-14}$	$-5.80(3)E^{-14}$
K (19, 39)	$-1.20571E^{-7}$	$-6.64768E^{-10}$	$-1.2837(15)E^{-7}$
K (19, 40)	$-1.20812E^{-7}$	$-6.66093E^{-10}$	$-1.286(2)E^{-7}$
K (19, 41)	$-1.21844E^{-7}$	$-6.71783E^{-10}$	$-1.297(4)E^{-7}$
Rb (37, 85)	$-1.24451E^{-5}$	$-1.78437E^{-8}$	$-1.3283(15)E^{-5}$
Rb (37, 87)	$-1.24169E^{-5}$	$-1.78034E^{-8}$	$-1.3254(13)E^{-5}$
Cs (55, 133)	$-2.65761E^{-4}$	$-1.68324E^{-7}$	$-2.842(5)E^{-4}$
Cs (55, 135)	$-2.66035E^{-4}$	$-1.68497E^{-7}$	$-2.845(5)E^{-4}$
Pb (82, 204)	$-9.41203E^{-3}$	$-2.52128E^{-6}$	$-1.0096(4)E^{-2}$
Pb (82, 206)	$-9.43977E^{-3}$	$-2.52871E^{-6}$	$-1.0125(4)E^{-2}$
Pb (82, 207)	$-9.45126E^{-3}$	$-2.53179E^{-6}$	$-1.0138(4)E^{-2}$
Pb (82, 208)	$-947062E^{-3}$	$-2.53698E^{-6}$	$-1.0159(4)E^{-2}$
Bi (83, 209)	$-1.06803E^{-2}$	$-2.78397E^{-6}$	$-1.1458(9)E^{-2}$
U (92, 235)	$-3.20879E^{-2}$	$-6.60084E^{-6}$	$-3.447(4)E^{-2}$
U (92, 236)	$-3.21652E^{-2}$	$-6.61674E^{-6}$	$-3.455(3)E^{-2}$
U (92, 238)	$-3.22805E^{-2}$	$-6.64045E^{-6}$	$-3.467(3)E^{-2}$

The correction $\varepsilon_{ba}^{(1)}$ in Eq. (74) can be written as

$$\varepsilon_{ba}^{(1)} = \int_0^{r_b} W_{ba}(r) [\varrho(r) - \varrho(0)] r^2 dr. \quad (76)$$

The correction to the ground state energy of model (b) is given in Eq. (76) and tabulated in Table VIII, which also tabulates the dimensionless corrections to the ground-state binding energy,

$$\delta_{ba} = \frac{\varepsilon_{ba}^{(1)}}{mc^2 - \varepsilon_1^{(0)}}, \quad (77)$$

where $\varepsilon_1^{(0)}$ is given in Eq. (21). For comparison, Table VIII shows $\varepsilon_{1,ba}$ and its uncertainty $\delta\varepsilon_{1,ba}$ calculated non-perturbatively from the equations,

$$\varepsilon_{1,ba} = \varepsilon_{1,b} - \varepsilon_{1,a}, \quad (78)$$

$$\delta\varepsilon_{1,ba} = \left| \frac{\partial \varepsilon_{1,ba}}{\partial r_N} \right| \delta r_N = \left| \delta\varepsilon_{1,b} - \delta\varepsilon_{1,a} \right|, \quad (79)$$

where $\delta\varepsilon_{1,a}$ and $\delta\varepsilon_{1,b}$ are given by

$$\delta\varepsilon_{1,a} = \left| \frac{\partial \varepsilon_{1,a}}{\partial r_N} \right| \delta r_N, \quad \delta\varepsilon_{1,b} = \left| \frac{\partial \varepsilon_{1,b}}{\partial r_N} \right| \delta r_N.$$

$\varepsilon_{1,a}$, $\delta\varepsilon_{1,a}$ and $\varepsilon_{1,b}$, $\delta\varepsilon_{1,b}$ are tabulated in Table III. Note that the first-order perturbation correction $\varepsilon_{ba}^{(1)}$ is close to the non-perturbative correction $\varepsilon_{1,ba}$ for all the isotopes. In other words, we conclude that the first-order perturbation correction $\varepsilon_{ba}^{(1)}$ gives accurate results for both light and heavy isotopes.

In summary, for light nuclei, perturbation theory gives results very close to the non-perturbative numerical calculations for the difference between $\varepsilon_{1,a}$ and $\varepsilon_{1,a}^{(1)}$, but for heavy isotopes the difference is large (see the large differences for the heavy isotopes between the values of $\varepsilon_{1,a}$ in Table III analytically calculated using model (a) and $\varepsilon_{1,a}^{(1)}$ calculated by perturbation theory using model (a) in Table VII).

V. TWO-PARAMETER FERMI MODEL FOR THE NUCLEAR CHARGE DISTRIBUTION

In model (c) the distribution of charge within the nucleus is taken to be the TPFM [24]. References [21, 22, 25] studied the FNS corrections to the hyperfine splitting of the ground state of H&HLI using a TPFM to parameterize the distribution of the nuclear charge. The TPFM is more realistic than either model (a) or (b), at least for heavier nuclei; but it is unclear how realistic it is for light nuclei. The TPFM charge distribution is,

$$\varrho_F(r) = \frac{Ze}{8\pi a_F^3 |\text{Li}_3(-e^{c_F/a_F})|} \left[\exp\left(\frac{r - c_F}{a_F}\right) + 1 \right]^{-1}, \quad (80)$$

where $\text{Li}_n(\bullet)$ is the polylogarithm function [47] of order n . Here c_F is the half-density nuclear radius, and a_F is the distribution thickness parameter. The charge density is normalized as follows:

$$4\pi \int_0^\infty \varrho_F(r) r^2 dr = Ze.$$

The nuclear charge radius is $r_N = \sqrt{\langle r^2 \rangle_N}$ is obtained by the expression,

$$\begin{aligned} r_N^2 \equiv \langle r^2 \rangle_N &= \frac{4\pi}{Ze} \int_0^\infty \varrho_F(r) r^4 dr \\ &= 12a_F^2 \frac{\text{Li}_5(-e^{c_F/a_F})}{\text{Li}_3(-e^{c_F/a_F})}. \end{aligned} \quad (81)$$

Note that the arguments of the polylogarithm functions contain an exponential function with argument c_F/a_F . We find c_F as a function of r_N and a_F using Eq. (81). The uncertainty δc_F in c_F due to the uncertainties δr_N and δa_F in r_N and a_F is,

$$\delta c_F = \sqrt{\left(\frac{\partial c_F}{\partial r_N} \delta r_N\right)^2 + \left(\frac{\partial c_F}{\partial a_F} \delta a_F\right)^2}. \quad (82)$$

TABLE IX. The half-density nuclear radii c_F (in Bohr), the distribution thickness parameter a_F (in Bohr), and the uncertainties δc_F and δa_F in c_F and a_F for a number of heavy isotopes. a_F and δa_F are taken from Ref. [24], c_F is calculated from Eq. (81), δc_F is calculated from Eq. (82), and r_N and δr_N are tabulated in Table I.

Isotope (Z, A)	c_F (δc_F)	a_F (δa_F)
Pb (82, 206)	1.2449(29) E^{-4}	1.030(15) E^{-5}
Pb (82, 207)	1.2456(36) E^{-4}	1.032(19) E^{-5}
Bi (83, 209)	1.278(12) E^{-4}	8.84(74) E^{-6}
U (92, 238)	1.3194(61) E^{-4}	1.143(30) E^{-5}

The nuclear charge radii r_N and their uncertainties δr_N for many nuclei are published in Ref. [24], and the parameters a_F and the uncertainties δa_F in a_F are published in Ref. [27]. As $a_F \rightarrow 0$, the charge distribution inside the nucleus becomes,

$$\lim_{a_F \rightarrow 0} \varrho_F(r) = \frac{3Ze}{4\pi r_b^3} \Theta(r_b - r), \quad \text{and } r_b = \lim_{a_F \rightarrow 0} c_F.$$

Figure 2 shows the charge density distribution versus r/r_N for three values of the width parameter, $a_F = 0.02 r_N, 0.1 r_N, 0.15 r_N$ (red, green and blue, respectively). Clearly, as $a_F \rightarrow 0$, the charge distribution approaches the limit given above. Moreover, in the limit as $a_F \rightarrow 0$, $c_F \rightarrow \sqrt{5/3} r_N$. The dashed black curve in Fig. 2 shows the charge density in this limit.

The TPFM charge distribution yields the following potential (for simplicity we have used c and a for a_F and c_F in this equation):

$$\begin{aligned} V_F(r) &= -\frac{Ze^2}{r} + \frac{4\pi}{r} \int_r^\infty \varrho_F(r') r' (r' - r) dr' = \\ &= Ze^2 \left[\frac{\text{Li}_3(-e^{\frac{c}{a} - \frac{r}{a}})}{r \text{Li}_3(-e^{\frac{c}{a}})} + \frac{\text{Li}_2(-e^{\frac{c}{a} - \frac{r}{a}})}{2a \text{Li}_3(-e^{\frac{c}{a}})} - \frac{1}{r} \right]. \end{aligned} \quad (83)$$

We numerically solve Dirac equation (13) for the heavy nuclei ^{206}Pb , ^{207}Pb , ^{209}Bi , and ^{238}U to obtain radial wave functions $g_n(r)$ and $f_n(r)$ and eigen-energies ε_n with potential (83) with c_F and a_F as tabulated in Table IX. The uncertainty $\delta\varepsilon_n$ in the energy ε_n of the ns state can be estimated as follows,

$$\delta\varepsilon_n = \sqrt{\left(\delta\varepsilon_n^{(r)}\right)^2 + \left(\delta\varepsilon_n^{(a)}\right)^2}, \quad (84)$$

where $\delta\varepsilon_n^{(r)}$ is the uncertainty in ε_n due to the uncertainty in r_N , and $\delta\varepsilon_n^{(a)}$ is the uncertainty in ε_n due to the uncertainty in a_F . $\delta\varepsilon_n^{(r)}$ and $\delta\varepsilon_n^{(a)}$ can be approxi-

TABLE X. The FNS corrections $\varepsilon_{n,c}$ to the energies ε_n of the ns states in Eq. (85), and the uncertainties $\delta\varepsilon_n$ in ε_n in Eq. (84).

Isotope (Z, A)	$\varepsilon_{1,c}$ ($\delta\varepsilon_1$)	$\varepsilon_{2,c}$ ($\delta\varepsilon_2$)
Pb (82, 206)	2.4605(10)	0.42724(17)
Pb (82, 207)	2.4634(10)	0.42774(17)
Bi (83, 209)	2.740(29)	0.4798(50)
U (92, 238)	7.2952(60)	1.3858(11)

mated as,

$$\begin{aligned} \delta\varepsilon_n^{(r)} &\approx \frac{1}{2} \left| \varepsilon_n(c_F(r_N + \delta r_N, a_F), a_F) \right. \\ &\quad \left. - \varepsilon_n(c_F(r_N - \delta r_N, a_F), a_F) \right|, \\ \delta\varepsilon_n^{(a)} &\approx \frac{1}{2} \left| \varepsilon_n(c_F(r_N, a_F + \delta a_F), a_F + \delta a_F) \right. \\ &\quad \left. - \varepsilon_n(c_F(r_N, a_F - \delta a_F), a_F - \delta a_F) \right|, \end{aligned}$$

where $\varepsilon_n(c_F(r_N \pm \delta r_N, a_F), a_F)$ is the ns state energy for the nuclear RMS charge radius $r_N \pm \delta r_N$, and $\varepsilon_n(c_F(r_N, a_F \pm \delta a_F), a_F \pm \delta a_F)$ is the ns state energy for the distribution thickness parameter $a_F \pm \delta a_F$. The FNS energy correction $\varepsilon_{n,c}$ is

$$\varepsilon_{n,c} = \varepsilon_n - \varepsilon_n^{(0)}, \quad (85)$$

where $\varepsilon_n^{(0)}$ is the energy of the ns state for a point-like nucleus. $\varepsilon_{n,c}$ and $\delta\varepsilon_n$ are tabulated in Table X for heavy isotopes. Comparing $\varepsilon_{n,c}$ with $\varepsilon_{n,a}$ and $\varepsilon_{n,b}$ in Tables III and IV, one sees that $\varepsilon_{n,a} > \varepsilon_{n,b} > \varepsilon_{n,c} > 0$ and $\varepsilon_{n,a} - \varepsilon_{n,b} > \varepsilon_{n,b} - \varepsilon_{n,c}$. For ^{206}Pb , ^{207}Pb and ^{238}U , the uncertainty $\delta\varepsilon_n$ in ε_n is the same for the models (a), (b) and (c). This is because $\delta\varepsilon_n^{(a)} \ll \varepsilon_n^{(r)}$, see Eq. (84). For ^{209}Bi , $\delta\varepsilon_n^{(a)}$ and $\varepsilon_n^{(r)}$ are of the same order of magnitude, and the uncertainty $\delta\varepsilon_n$ for the model (c) is larger than the uncertainty for models (a) and (b).

VI. GROUND STATE HYPERFINE SPLITTING

Within the Dirac equation formalism, the hyperfine interaction between the magnetic moments of the electron (located at space point \mathbf{r}) and the nucleus (located at the origin) can be expressed in terms of the vector potential $\mathbf{A}(\mathbf{r})$. The interaction Hamiltonian is

$$H_{\text{mag}} = [c] e \boldsymbol{\alpha} \cdot \mathbf{A}(\mathbf{r}), \quad (86)$$

where the factor $[c]$ is present in SI units but is unity in Gaussian units, and $\mathbf{A}(\mathbf{r})$ is the vector potential generated by the magnetic moment of the nucleus with magnetic moment density $\boldsymbol{\mu}(\mathbf{r}')$,

$$\mathbf{A}_\nu(\mathbf{r}) = \left[\frac{\mu_0}{4\pi} \right] \int \frac{\boldsymbol{\mu}_\nu(\mathbf{r}') \times (\mathbf{r} - \mathbf{r}')}{|\mathbf{r} - \mathbf{r}'|^3} d^3\mathbf{r}', \quad (87)$$

where integration is over all space. The subscript ν specifies the models for the magnetic moment distribution: $\nu = 0, a, b, c$ are the point-like, uniform surface, uniform volume, and TPFM. Here the factor $\left[\frac{\mu_0}{4\pi} \right]$ is present in SI units but is unity in Gaussian units. We restrict ourselves by considering isotropic models where the magnetic moment density $\boldsymbol{\mu}(\mathbf{r}')$ depends only on the distance $r' = |\mathbf{r}'|$ from the center of mass of the nucleus. For the point-like distribution, $\nu = 0$,

$$\boldsymbol{\mu}_0(r) = g_I \mu_N \mathbf{I} \delta^3(\mathbf{r}), \quad (88)$$

where μ_N is the nuclear magneton, $\mu_N = e\hbar/(2m_p c)$ in Gaussian units, m_p is the proton mass, g_I is the nuclear g -factor, \mathbf{I} is the nuclear spin operator, and $\delta^3(\mathbf{r})$ is the three dimensional Dirac delta function. For $\nu = a$,

$$\boldsymbol{\mu}_a(r) = \frac{g_I \mu_N}{4\pi r_a^2} \mathbf{I} \delta(r - r_a), \quad (89)$$

where $\delta(\bullet)$ is the Dirac δ function. For $\nu = b$,

$$\boldsymbol{\mu}_b(r) = \frac{3g_I \mu_N}{4\pi r_b^3} \mathbf{I} \Theta(r_b - r). \quad (90)$$

For the Fermi model, $\nu = c$,

$$\boldsymbol{\mu}_c(r) = \frac{\vartheta_0}{e^{(r-c_F)/a_F} + 1} g_I \mu_N \mathbf{I}. \quad (91)$$

The factor ϑ_0 is determined from the normalization condition,

$$4\pi\vartheta_0 \int_0^\infty \frac{r^2 dr}{e^{(r-c_F)/a_F} + 1} = 1.$$

This yields,

$$\vartheta_0 = -\frac{1}{8\pi a_F^3 \text{Li}_3(-e^{c_F/a_F})}.$$

Substituting $\boldsymbol{\mu}_\nu(r')$ into Eq. (87), we get,

$$\mathbf{A}_\nu(\mathbf{r}) = \left[\frac{\mu_0}{4\pi} \right] \frac{g_I \mu_N}{r^2} [\mathbf{I} \times \mathbf{e}_r] \mathcal{M}_\nu(r), \quad (92)$$

where

$$\mathcal{M}_0(r) = 1, \quad (93)$$

$$\mathcal{M}_a(r) = \Theta(r - r_a), \quad (94)$$

$$\mathcal{M}_b(r) = \frac{r^3}{r_b^3} \Theta(r_b - r) + \Theta(r - r_b). \quad (95)$$

$$\begin{aligned} \mathcal{M}_c(r) &= 4\pi\vartheta_0 \int_0^r \frac{r'^2 dr'}{e^{(r'-c_F)/a_F} + 1} \\ &= \frac{1}{\text{Li}_3(-e^{c_F/a_F})} \left[\frac{r^2}{2a^2} \ln(1 + e^{(c_F-r)/a_F}) \right. \\ &\quad \left. + \text{Li}_3(-e^{c_F/a_F}) - \text{Li}_3(-e^{(c_F-r)/a_F}) \right. \\ &\quad \left. - \frac{r}{a_F} \text{Li}_2(-e^{(c_F-r)/a_F}) \right]. \quad (96) \end{aligned}$$

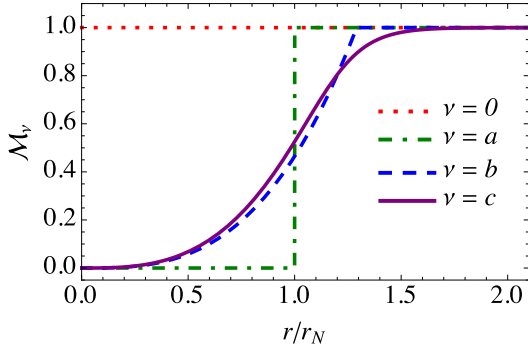


FIG. 7. $\mathcal{M}_\nu(r)$ versus r for ^{207}Pb nucleus for different magnetic moment distribution models: The point-like nucleus, $\nu = 0$ (red dotted curve), distributed homogeneously on a sphere of radius r_a , $\nu = a$ (green dot-dashed curve), distributed homogeneously inside a sphere of radius r_b , $\nu = b$ (dashed blue curve), and the TPFM in Eq. (96), $\nu = c$ (solid purple curve).

The function $\mathcal{M}_\nu(r)$ is plotted versus r in Fig. 7 for the four magnetic moment distribution models. Substituting Eq. (92) into Eq. (86), we obtain

$$H_{\text{hf}}^{(\nu)} = \left[\frac{\mu_0 c}{4\pi} \right] \frac{egI\mu_N}{r^2} \mathcal{M}_\nu(r) \left(\mathbf{I} \cdot [\mathbf{e}_r \times \boldsymbol{\alpha}] \right). \quad (97)$$

Assuming that the hyperfine splitting of the ground state is much smaller than the excitation energy of the $2p$ state, we can restrict ourselves to first-order perturbation theory,

$$\epsilon_{\text{hf}}^{(\nu)}(F) = \langle \Psi_{F, m_F}^{(\nu)} | H_{\text{hf}}^{(\nu)} | \Psi_{F, m_F}^{(\nu)} \rangle, \quad (98)$$

where the ground-state wave function $|\Psi_{F, m_F}^{(\nu)}\rangle$ is

$$\begin{aligned} \langle \mathbf{r} | \Psi_{F, m_F}^{(\nu)} \rangle &= \sum_{m_J, m_I} \langle \frac{1}{2}, m_J; I, m_I | F, m_F \rangle \\ &\times \langle \mathbf{r} | \nu; \frac{1}{2}, m_J; I, m_I \rangle, \end{aligned} \quad (99)$$

$|\nu; \frac{1}{2}, m_J; I, m_I\rangle$ is the atomic angular ket with total electronic angular momentum vector \mathbf{J} ($J = 1/2$) and projection $m_J = \pm \frac{1}{2}$, nuclear spin \mathbf{I} , and projection m_I , and

$$\langle \mathbf{r} | \nu; \frac{1}{2}, m_J; I, m_I \rangle = \chi_{I, m_I} \psi_{m_J}^{(\nu)}(\mathbf{r}),$$

χ_{I, m_I} is a nuclear spin wave function, and $\psi_{m_J}^{(\nu)}(\mathbf{r})$ is a spatial wave function,

$$\psi_{m_J}^{(\nu)}(\mathbf{r}) = \begin{pmatrix} g_\nu(r) \Omega_{\frac{1}{2} 0 m_J} \\ i f_\nu(r) \Omega_{\frac{1}{2} 1 m_J} \end{pmatrix}. \quad (100)$$

For $\nu = 0$, the radial wave functions $g_0(r)$ and $f_0(r)$ are given in Eq. (23). For $\nu = a$, the radial wave functions $g_a(r)$ and $f_a(r)$ are

$$g_a(r) = g_+(r)\Theta(r - r_a) + g_-(r)\Theta(r_a - r), \quad (101a)$$

$$f_a(r) = f_+(r)\Theta(r - r_a) + f_-(r)\Theta(r_a - r), \quad (101b)$$

where $g_+(r)$ and $f_+(r)$ are given in Eq. (27), and $g_-(r)$ and $f_-(r)$ are given in Eq. (45). For $\nu = b$, the wave functions ($g_b(r)$, $f_b(r)$) are numerically calculated as described in Sec. III C, and for $\nu = c$ the wave functions must be numerically calculated using the Dirac equation for a potential which includes a two-parameter Fermi nuclear model distribution.

Substituting Eq. (99) into Eq. (98), we find $\epsilon_{\text{hf}}^{(\nu)}(F)$,

$$\epsilon_{\text{hf}}^{(\nu)}(F) = \frac{\Delta_\nu}{2} [F(F+1) - I(I+1) - S(S+1)], \quad (102)$$

where $S = 1/2$. The hyperfine splitting $\Delta_\nu = \epsilon_{\text{hf}}^{(\nu)}(I + 1/2) - \epsilon_{\text{hf}}^{(\nu)}(I - 1/2)$ is

$$\begin{aligned} \Delta_\nu &= - \left[\frac{\mu_0 c}{4\pi} \right] \left(I + \frac{1}{2} \right) \frac{8egI\mu_N}{3} \\ &\times \int_0^\infty \mathcal{M}_\nu(r) g_\nu(r) f_\nu(r) dr. \end{aligned} \quad (103)$$

The expression for the hyperfine splitting of the ground state of H&HLI given in Ref. [21] is equivalent to

$$\begin{aligned} \Delta &= \frac{4mc^2}{3} \frac{\alpha(Z\alpha)^3}{\gamma(2\gamma-1)} g_I \frac{m_e}{m_p} \left(I + \frac{1}{2} \right) \\ &\times \left[(1-\xi)(1-\eta) + \zeta_{\text{QED}} \right]. \end{aligned} \quad (104)$$

Note the use of the electron reduced mass m in Eq. (104), as discussed in Refs. [30–33]. In the following we shall write Eq. (104) in the form

$$\Delta = \Delta_0 \left[(1-\xi)(1-\eta) + \zeta_{\text{QED}} \right], \quad (105)$$

where

$$\Delta_0 = \frac{4mc^2}{3} \alpha(Z\alpha)^3 g_I \frac{m_e}{m_p} \left(I + \frac{1}{2} \right) \frac{1}{\gamma(2\gamma-1)}. \quad (106)$$

Δ_0 is the well-known uncorrected relativistic hyperfine splitting [21]. Here ξ and η are the FNS corrections to the hyperfine splitting due to the charge distribution and the magnetic moment distribution (Bohr-Weisskopf correction) respectively [see Eqs. (109), (113) and (117), and the text below for models (a), (b) and (c)], and the quantity ζ_{QED} is the QED radiative correction to the hyperfine splitting. Relativistic QED radiative corrections are addressed in Ref. [21], where a quantity χ_{QED} is defined. We prefer to present the QED radiative correction in terms of the quantity $\zeta_{\text{QED}} \equiv \gamma(2\gamma-1)\chi_{\text{QED}}$ because ζ_{QED} can be directly compared with ξ and η , as is clear from Eq. (104). Note that we do not calculate the QED radiative corrections here but rather use values reported in the literature.

Below, we calculate hyperfine splitting for the four models $\nu = 0, a, b, c$ for the *magnetic moment distribution*. We should point out that the nuclear magnetic

TABLE XI. Nuclear g_I , nuclear spin I , and ground-state hyperfine splitting Δ_0 calculated using Eq. (106) [in Hartree], for point-like nuclei. The nuclear g factors for ^1H , ^2H , ^3H and ^3He nuclei are taken from 2018 CODATA, i.e., Ref. [10], and those for ^{39}K , ^{40}K , ^{41}K , ^{85}Rb , ^{87}Rb , ^{133}Cs are taken from Ref. [56], those for ^{135}Cs and ^{235}U are taken from Ref. [58], those for ^{207}Pb and ^{209}Bi are taken from Ref. [57].

Isotope (Z, A)	g_I	I	Δ_0
H (1, 1)	5.5856946893(16)	1/2	$2.1589180648(6)E^{-7}$
H (1, 2)	0.8574382338(22)	1	$4.972458067(13)E^{-8}$
H (1, 3)	5.957924931(12)	1/2	$2.3036226460(46)E^{-7}$
He (2, 3)	-4.255250615(50)	1/2	$1.316544463(15)E^{-8}$
K (19, 39)	0.26061413(22)	3/2	$1.4234088(12)E^{-4}$
K (19, 40)	-0.324063(62)	4	$-3.98239(77)E^{-4}$
K (19, 41)	0.14304731(15)	3/2	$7.812889(8)E^{-5}$
Rb (37, 85)	0.5391679(11)	5/2	$3.554396(7)E^{-3}$
Rb (37, 87)	1.8272315(18)	3/2	$8.030529(8)E^{-3}$
Cs (55, 133)	0.732356746(95)	7/2	$2.4735911(32)E^{-2}$
Cs (55, 135)	0.78069(6)	7/2	$2.63683(19)E^{-2}$
Pb (82, 207)	1.16438(4)	1/2	$5.1434(2)E^{-2}$
Bi (83, 209)	0.91347(4)	9/2	$2.14590(10)E^{-1}$
U (92, 235)	-0.109(9)	7/2	$-3.66(29)E^{-2}$

moment distribution can be very different from the nuclear charge distribution. This is particularly true for nuclei with one nucleon outside a closed nuclear shell. Appendix D discusses this case. In our calculations we used the same distribution for both nuclear charge and nuclear magnetic moment.

A. Point-like charge and magnetic moment

Numerical values of Δ_0 are tabulated in Table XI for a number of isotopes. For some ions, g_I is negative, and the hyperfine interaction is ferromagnetic, hence $\Delta_0 < 0$. Figure 8 plots the magnitude of the uncorrected hyperfine splitting versus A .

B. Charge and magnetic moment distributions for model (a)

Substituting Eqs. (94) and (101) into Eq. (103) with $\nu = a$, we find

$$\Delta_a = -\frac{4mc^2}{3} \alpha(Z\alpha)^3 g_I \frac{m_e}{m_p} \left(I + \frac{1}{2}\right) \times a_B^2 \int_{r_a}^{\infty} g_+(r) f_+(r) dr. \quad (107)$$

As in Eq. (105), it is convenient to write Δ_a in the form

$$\Delta_a = \Delta_0 (1 - \xi_a) (1 - \eta_a), \quad (108)$$

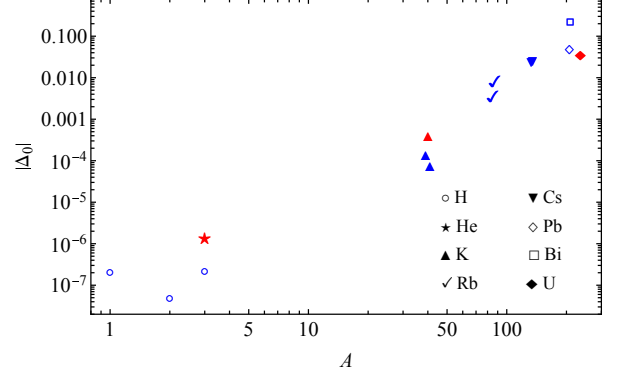


FIG. 8. Absolute value of the hyperfine splitting $|\Delta_0|$ (in Hartree) in Eq. (106) for a point-like nucleus versus A . Positive values of the hyperfine splitting Δ_0 (positive g_I) are marked by blue symbols, and negative values of Δ_0 (negative g_I) are shown in red.

where Δ_0 is given in Eq. (106). The corrections ξ_a and η_a are calculate within model (a). Explicitly,

$$\xi_a = \frac{\mathcal{G}_0 - \mathcal{G}_a}{\mathcal{G}_0}, \quad \eta_a = \frac{\mathcal{G}_-^{(a)}}{\mathcal{G}_a}, \quad (109)$$

where

$$\mathcal{G}_0 = \frac{a_B^2}{Z^3 \alpha} \int_0^{\infty} g_0(r) f_0(r) dr = -\frac{1}{\gamma(2\gamma - 1)}, \quad (110a)$$

$$\mathcal{G}_-^{(a)} = \frac{a_B^2}{Z^3 \alpha} \int_0^{r_a} g_{a,-}(r) f_{a,-}(r) dr, \quad (110b)$$

$$\mathcal{G}_a = \mathcal{G}_-^{(a)} + \frac{a_B^2}{Z^3 \alpha} \int_{r_a}^{\infty} g_+(r) f_+(r) dr. \quad (110c)$$

The corrections ξ_a and ξ_b are tabulated in Table XII, and η_a and η_b are tabulated in Table XIII. Here the numbers in the parenthesis are the uncertainties. For example, ξ_a for the ^1H isotope is

$$\xi_a = 1.1092(2)E^{-3} \equiv (1.1092 \pm 0.0002) \times 10^{-3}.$$

For all the isotopes, $|\xi_a - \xi_b|$ is larger than the uncertainties in ξ_a and ξ_b , and $|\eta_a - \eta_b|$ is much larger than the uncertainties in η_a and η_b . Thus the ground-state hyperfine splitting is very sensitive to the nuclear charge and magnetic moment distribution.

TABLE XII. The corrections ξ_a and ξ_b to the hyperfine splitting for models (a) [Eq. (109)], and (b) [Eq. (113)].

Isotope (Z, A)	ξ_a	ξ_b
H (1, 1)	$1.1092(2)E^{-3}$	$1.1106(2)E^{-3}$
H (1, 2)	$5.9912(2)E^{-4}$	$6.0261(2)E^{-4}$
H (1, 3)	$4.087(9)E^{-4}$	$4.116(10)E^{-4}$
He (2, 3)	$5.126(2)E^{-4}$	$5.0786(10)E^{-4}$
K (19, 39)	$2.8513(15)E^{-3}$	$2.7643(7)E^{-3}$
K (19, 40)	$2.853(2)E^{-3}$	$2.7661(10)E^{-3}$
K (19, 41)	$2.864(4)E^{-3}$	$2.776(2)E^{-3}$
Rb (37, 85)	$9.173(5)E^{-3}$	$8.911(2)E^{-3}$
Rb (37, 87)	$9.163(4)E^{-3}$	$8.902(2)E^{-3}$
Cs (55, 133)	$2.4526(19)E^{-2}$	$2.3913(9)E^{-2}$
Cs (55, 135)	$2.454(2)E^{-2}$	$2.3924(9)E^{-2}$
Pb (82, 207)	$0.107053(17)$	$0.105226(7)$
Bi (83, 209)	$0.11338(3)$	$0.111483(13)$
U (92, 235)	$0.19317(6)$	$0.19062(3)$

TABLE XIII. The corrections η_a and η_b to the hyperfine splitting for models (a) [Eq. (109)], and (b) [Eq. (113)].

Isotope (Z, A)	η_a	η_b
H (1, 1)	$1.060(11)E^{-5}$	$1.847(19)E^{-5}$
H (1, 2)	$2.6812(9)E^{-5}$	$4.6729(16)E^{-5}$
H (1, 3)	$2.22(5)E^{-5}$	$3.86(8)E^{-5}$
He (2, 3)	$4.961(8)E^{-5}$	$8.646(13)E^{-5}$
K (19, 39)	$9.083(5)E^{-4}$	$1.5807(9)E^{-3}$
K (19, 40)	$9.092(7)E^{-4}$	$1.5822(13)E^{-3}$
K (19, 41)	$9.127(14)E^{-4}$	$1.588(2)E^{-3}$
Rb (37, 85)	$2.6911(14)E^{-3}$	$4.665(3)E^{-3}$
Rb (37, 87)	$2.6883(12)E^{-3}$	$4.660(2)E^{-3}$
Cs (55, 133)	$6.179(5)E^{-3}$	$1.0645(9)E^{-2}$
Cs (55, 135)	$6.182(5)E^{-3}$	$1.0650(9)E^{-2}$
Pb (82, 207)	$1.8471(3)E^{-2}$	$3.1386(6)E^{-2}$
Bi (83, 209)	$1.9209(6)E^{-2}$	$3.2619(11)E^{-2}$
U (92, 235)	$2.7368(11)E^{-2}$	$4.620(2)E^{-2}$

C. Charge and magnetic moment distribution inside the nucleus for model (b)

Substituting Eqs. (95) and (101) into Eq. (103) with $\nu = b$, we get

$$\Delta_b = -\frac{4mc^2}{3} \alpha (Z\alpha)^3 g_I \frac{m_e}{m_p} \left(I + \frac{1}{2} \right) \times \left\{ a_B^2 \int_0^{r_b} \frac{r^3}{r_b^3} g_{b,-}(r) f_{b,-}(r) dr + a_B^2 \int_{r_b}^{\infty} g_{+}(r) f_{+}(r) dr \right\}. \quad (111)$$

We write Δ_b in the form

$$\Delta_b = \Delta_0 (1 - \xi_b) (1 - \eta_b), \quad (112)$$

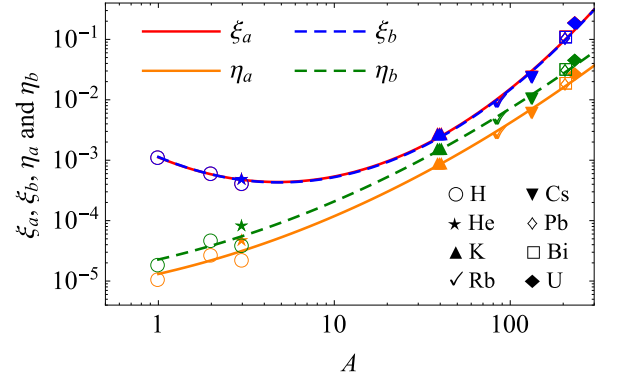


FIG. 9. Corrections to the ground-state hyperfine splitting due to FNS distributions of the nuclear charge and magnetic moment as a function of the atomic mass number A . The corrections ξ_a and η_a [red and orange] are defined in Eq. (109) and the correction ξ_b and η_b [blue and green] is defined in Eq. (113) [blue]. The solid curves that fit the data for ξ_a , η_a and ξ_b , η_b are meant to guide the eye (see the text). Redo figure.

where Δ_0 is defined in Eq. (106),

$$\xi_b = \frac{\mathcal{G}_0 - \mathcal{G}_b}{\mathcal{G}_0}, \quad \eta_b = \frac{\mathcal{G}_-^{(b)} - \mathcal{F}_-^{(b)}}{\mathcal{G}_b}, \quad (113)$$

\mathcal{G}_0 is given in Eq. (110a), and

$$\mathcal{F}_-^{(b)} = \frac{a_B^2}{Z^3 \alpha} \int_0^{r_b} \frac{r^3}{r_b^3} g_{b,-}(r) f_{b,-}(r) dr, \quad (114a)$$

$$\mathcal{G}_-^{(b)} = \frac{a_B^2}{Z^3 \alpha} \int_0^{r_b} g_{b,-}(r) f_{b,-}(r) dr, \quad (114b)$$

$$\mathcal{G}_b = \mathcal{G}_-^{(b)} + \frac{a_B^2}{Z^3 \alpha} \int_{r_b}^{\infty} g_{+}(r) f_{+}(r) dr. \quad (114c)$$

D. FNS corrections to hyperfine splitting in models (a) and (b)

The FNS corrections to the hyperfine splitting ξ_a , ξ_b , η_a and η_b are tabulated in Tables XII and XIII and are plotted in Fig. 9 as functions of A . Numerical analysis shows that $\ln \xi_a$, $\ln \eta_a$, $\ln \xi_b$ and $\ln \eta_b$ can be well-fit by

$$\ln \xi_a(A) = -6.79743 - 1.20214 \ln A + 0.384078 \ln^2 A, \quad (115a)$$

$$\ln \eta_a(A) = -11.2423 + 0.661711 \ln A + 0.128055 \ln^2 A, \quad (115b)$$

$$\ln \xi_b(A) = -6.78386 - 1.22495 \ln A + 0.38719 \ln^2 A, \quad (115c)$$

$$\ln \eta_b(A) = -10.6924 + 0.673483 \ln A + 0.125229 \ln^2 A. \quad (115d)$$

FNS corrections to the hyperfine splitting of the ground state of heavy HLI were calculated in Ref. [22]. The corrections ξ_a for ^{207}Pb and ^{209}Bi in Table XII are not far from the values calculated in Ref. [22], $\xi(\text{Pb}) = 0.1049$, and $\xi(\text{Bi}) = 0.1111$, the values of η_a for ^{209}Bi in Table XIII not far from the value reported in [22], $\epsilon = 0.0118$, and η_b for ^{207}Pb not too far away from $\epsilon = 0.0419$ in Ref. [22].

Within the assumption that $W_{ba}(r)$ in Eq. (7) is small [i.e., $W_{ba}(r)$ is much weaker than $W_a(r)$ or $W_b(r)$ in Eq. (6), see Fig. 1], we showed that the correction ξ is almost the same for both models (a) and (b), whereas models (a) and (b) predict very different values for the corrections η_ν due to the magnetic moment distribution.

E. Charge and magnetic moment distribution inside the nucleus for model (c)

For the TPFM, model (c),

$$\Delta_c = \Delta_0(1 - \xi_c)(1 - \eta_c), \quad (116)$$

where Δ_0 is given in (106),

$$\xi_c = \frac{\mathcal{G}_0 - \mathcal{G}_c}{\mathcal{G}_0}, \quad \eta_c = \frac{\mathcal{F}_c}{\mathcal{G}_c}, \quad (117)$$

and

$$\mathcal{G}_c = \frac{a_B^2}{Z^3 \alpha} \int_0^\infty g_c(r) f_c(r) dr, \quad (118a)$$

$$\mathcal{F}_c = \frac{a_B^2}{Z^3 \alpha} \int_0^\infty [1 - \mathcal{M}_c(r)] g_c(r) f_c(r) dr. \quad (118b)$$

F. Relativistic QED radiative corrections for hyperfine splitting

We now include the relativistic QED radiative corrections $\zeta_{\text{QED}} = \gamma(2\gamma - 1)\chi_{\text{QED}}$ given in Eq. (105). The quantity χ_{QED} is calculated in Refs. [22, 25] for some elements. The corrections ζ_{QED} are tabulated in Table XIV.

We fit ζ_{QED} by the formula [25],

$$\zeta_{\text{QED}}^{(\text{fit})}(Z) = \frac{\alpha}{\pi} \left[A_0 - A_1 \alpha Z + A_2 (\alpha Z)^2 + A_3 (\alpha Z)^2 \ln(\alpha Z) + A_4 (\alpha Z \ln(\alpha Z))^2 \right], \quad (119)$$

The fit gives,

$$\begin{aligned} A_0 &= 0.509092 \\ A_1 &= 7.08715, \\ A_2 &= 4.43975, \\ A_3 &= 0.696079, \\ A_4 &= 0.448402, \end{aligned}$$

TABLE XIV. Radiative QED correction $\zeta_{\text{QED}} = \gamma(2\gamma - 1)\chi_{\text{QED}}$ to the hyperfine splitting in Eq. (105), where γ is given in Eq. (15) and χ_{QED} is calculated in Refs. [22, 25] for some elements. The fit $\zeta_{\text{QED}}^{(\text{fit})}$ is calculated using Eq. (119).

Z	ζ_{QED}	$\zeta_{\text{QED}}^{(\text{fit})}$
1	0.00105756	0.00106387
2		0.000946973
3	0.000835844	0.000831409
5	0.000609149	0.000603679
7	0.000382069	0.00038002
10	0.0000466108	0.0000516092
19		-0.000884945
37		-0.00253464
49	-0.00348472	-0.00345706
53	-0.00373754	-0.00373092
55		-0.00386134
57	-0.0039463	-0.00398737
63	-0.00427325	-0.00433865
67	-0.00467521	-0.00455007
71	-0.00461933	-0.00474287
75	-0.00501339	-0.00491674
82	-0.0051733	-0.0051745
83	-0.0051822	-0.00520641
92		-0.00543714

and the mean standard deviation σ_{QED} is

$$\begin{aligned} \sigma_{\text{QED}} &= \left(\frac{1}{N_Z} \sum_{n_Z} (\zeta_{\text{QED}}(Z) - \zeta_{\text{QED}}^{(\text{fit})}(Z))^2 \right)^{1/2} \\ &= 0.000058397, \end{aligned}$$

where ζ_{QED} was taken from Table XIV, $N_Z = 14$ is the number of elements for which ζ_{QED} is tabulated in the table, and n_Z is a running index over the elements used. The QED radiative correction ζ_{QED} and its fit using Eq. (119) are shown in Fig. 10. The fit (blue curve) is close to the red dots, hence we conclude that the approximation in Eq. (119) is satisfactory. The QED radiative corrections $\zeta_{\text{QED}}^{(\text{fit})}(Z)$ in Eq. (119) are tabulated in Table XIV for H&HLI. For heavy isotopes, $\zeta_{\text{QED}}(Z)$ satisfies the inequalities: $\zeta_{\text{QED}} < 0$, and $\eta_a < |\zeta_{\text{QED}}| < \eta_b \ll \xi$, where ξ_a and ξ_b are tabulated in Table XII, and η_a and η_b are tabulated in Table XIII. Therefore, we conclude that the main contribution to the hyperfine splitting is the correction ξ due to the finite nuclear charge distribution, which is much larger than the relativistic QED radiative corrections and the correction of the magnetic momentum distribution due to FNS. For light elements (e.g., H and He), $\zeta_{\text{QED}} > 0$ and satisfies the inequalities, $\zeta_{\text{QED}} > \xi_a, \xi_b > \eta_a, \eta_b$, i.e., the QED radiative corrections to the ground-state hyperfine splitting are larger than the FNS effects. For heavy elements, $\zeta_{\text{QED}} < 0$ and satisfies the inequalities, $|\zeta_{\text{QED}}| < \eta_a, \eta_b < \xi_a, \xi_b$; The FNS corrections to the hyperfine splitting due to the charge distribution are the largest correction using

either model (a) or (b).

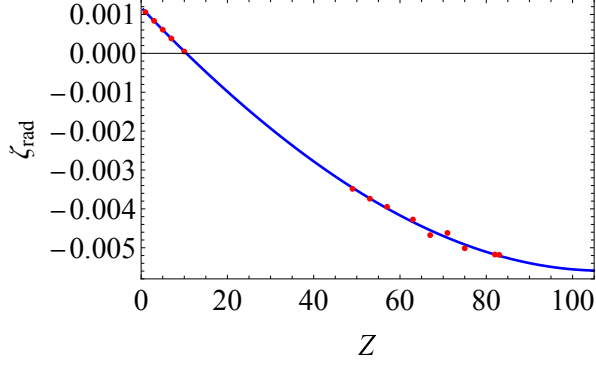


FIG. 10. Radiative QED correction (red dots) $\zeta_{\text{QED}} = \gamma(2\gamma - 1)\chi_{\text{QED}}$ to the hyperfine splitting in Eq. (105), versus nuclear charge Z where χ_{QED} is calculated in Refs. [22, 25]. The blue curve is the fit of ζ_{QED} in Eq. (119).

VII. ESTIMATES OF THE UNCERTAINTY OF THE HYPERFINE SPLITTING IN MODELS (a), (b) AND (c)

The ground-state hyperfine splittings Δ_a , Eq. (108), and Δ_b , Eq. (112), depend on the nuclear g factor g_I and the RMS nuclear charge radius r_N . Both g_I and r_N are measured in experiment with their uncertainties δg_I and δr_N , see Tables I and XI. The uncertainties δg_I and δr_N give rise to uncertainties $\delta\Delta_a$ and $\delta\Delta_b$ that are given by

$$\delta\Delta_\nu = \sqrt{\left(\frac{\partial\Delta_\nu}{\partial g_I} \delta g_I\right)^2 + \left(\frac{\partial\Delta_\nu}{\partial r_N} \delta r_N\right)^2}. \quad (120)$$

Using Eq. (108) and (112), we can write Eq. (120) as,

$$\delta\Delta_\nu = \Delta_\nu \sqrt{\left(\frac{\delta g_I}{g_I}\right)^2 + \left(\frac{\delta\xi_\nu}{1-\xi_\nu} + \frac{\delta\eta_\nu}{1-\eta_\nu}\right)^2}. \quad (121)$$

The ground-state hyperfine splitting Δ_c in Eq. (116) depends on g_I , r_N and the distribution thickness parameter a_F . The parameters g_I , r_N and a_F , and their uncertainties δg_I , δr_N and δa_F , are measured in experiment, see Tables I, IX and XI. The uncertainty $\delta\Delta_c$ in Δ_c due to the uncertainties δg_I , δr_N and δa_F is estimated as,

$$\delta\Delta_c = \sqrt{\left(\frac{\partial\Delta_c}{\partial g_I} \delta g_I\right)^2 + \left(\frac{\partial\Delta_c}{\partial r_N} \delta r_N\right)^2 + \left(\frac{\partial\Delta_c}{\partial a_F} \delta a_F\right)^2}. \quad (122)$$

Using Eq. (116), we can rewrite Eq. (122) in the form,

$$\delta\Delta_c = \left[\left(\frac{\delta g_I}{g_I}\right)^2 + \left(\frac{\delta\xi_c^{(r)}}{1-\xi_c} + \frac{\delta\eta_c^{(r)}}{1-\eta_c}\right)^2 + \left(\frac{\delta\xi_c^{(a)}}{1-\xi_c} + \frac{\delta\eta_c^{(a)}}{1-\eta_c}\right)^2 \right]^{1/2}, \quad (123)$$

where $\delta\xi_c^{(r)}$ and $\delta\xi_c^{(a)}$ are the uncertainties in ξ_c due to the uncertainties δr_N and δa_F in r_N and a_F ,

$$\delta\xi_c^{(r)} = \left| \frac{\partial\xi_c}{\partial r_N} \right| \delta r_N, \quad \delta\xi_c^{(a)} = \left| \frac{\partial\xi_c}{\partial a_F} \right| \delta a_F,$$

and $\delta\eta_c^{(r)}$ and $\delta\eta_c^{(a)}$ are the uncertainties in η_c due to the uncertainties δr_N and δa_F in r_N and a_F ,

$$\delta\eta_c^{(r)} = \left| \frac{\partial\eta_c}{\partial r_N} \right| \delta r_N, \quad \delta\eta_c^{(a)} = \left| \frac{\partial\eta_c}{\partial a_F} \right| \delta a_F.$$

VIII. HYPERFINE SPLITTING: COMPARISON WITH EXPERIMENT

We now compare the results of experiments on the ground state hyperfine splitting of H&HLI with the results of our calculations using model (a) and (b). We present results of the calculations without and with relativistic QED radiative corrections.

The percent uncertainties of the theoretical results compared with the experimental values are defined as,

$$\tau_\nu = \frac{\Delta_{\text{exp}} - \tilde{\Delta}_\nu}{\Delta_{\text{exp}}}, \quad (124)$$

where $\nu = a, b, c$, and $\tilde{\Delta}_\nu$ is a hyperfine splitting with the QED radiative correction given by

$$\tilde{\Delta}_\nu = \Delta_0 \left[(1 - \xi_\nu)(1 - \eta_\nu) + \zeta_{\text{QED}} \right] = \Delta_\nu + \Delta_0 \zeta_{\text{QED}}. \quad (125)$$

The experimental hyperfine splitting Δ_{exp} for hydrogen atoms and helium ions are taken from Refs. [48–52], values for hydrogenic lead ions are taken from Ref. [53], and values for hydrogenic bismuth ions are taken from Ref. [54]. The quantities $\tilde{\Delta}_a$, $\tilde{\Delta}_b$, Δ_{exp} , τ_a and τ_b are tabulated in Table XV. For ^1H atoms and ^3He ions, $\tau_a < 0$ and $\tau_b > 0$, and $\tilde{\Delta}_a < \Delta_{\text{exp}} < \tilde{\Delta}_b$. Moreover, $|\tau_a|$ and τ_b are smaller than the FNS corrections η_ν and ξ_ν and the QED radiative correction ζ_{QED} . For ^2H and ^3H atoms, both τ_a and τ_b are positive, and $\tilde{\Delta}_a$ and $\tilde{\Delta}_b$ are below Δ_{exp} . Moreover, τ_a and τ_b exceed η_ν , but are below ξ_ν and ζ_{QED} . For ^{207}Pb ions, $\tau_a < 0$ and $\tau_b > 0$, and for ^{209}Bi ions, $\tau_a > 0$ and $\tau_b > 0$. For both ^{207}Pb and ^{209}Bi , $|\tau_a|$ and τ_b are below η_ν and ξ_ν , but above ζ_{QED} .

TABLE XV. Experimental values of the hyperfine splitting Δ_{exp} [in Hartree], as compared with the calculated results $\tilde{\Delta}_a$ and $\tilde{\Delta}_b$ in Eq. (125) using models (a) and (b) with relativistic QED radiative corrections, and the percent uncertainties ($\tilde{\tau}_a, \tilde{\tau}_b$) of theoretical results compared with Δ_{exp} . The numbers in brackets show uncertainty $\delta\Delta_{\text{exp}}$ in Δ_{exp} , and $\delta\Delta_\nu$ in Δ_ν with $\nu = a, b$, see Eq. (121). The experimental values for hydrogen atoms and helium ions are taken from Refs. [48–52], values for hydrogenic lead ions are taken from Ref. [53] and values for hydrogenic bismuth ions are taken from Ref. [54]. The percent uncertainties τ_ν of the theoretical results compared with the experimental values [see Eq. (124)]. The model (c) results for heavy ions are not presented in this table; they are presented below.

Isotope (Z, A)	$\tilde{\Delta}_a$	$\delta\tilde{\Delta}_a/\tilde{\Delta}_a$	$\tilde{\Delta}_b$	$\delta\tilde{\Delta}_b/\tilde{\Delta}_b$	Δ_{exp}	τ_a	τ_b
H (1, 1)	$2.1587837(7)E^{-7}$	$3E^{-7}$	$2.1587637(8)E^{-7}$	$4E^{-7}$	$2.158775054569(2)E^{-7}$	$-4.0E^{-6}$	$5.2E^{-6}$
H (1, 2)	$4.97460440(14)E^{-8}$	$3E^{-8}$	$4.97448807(18)E^{-8}$	$4E^{-8}$	$4.9756850998(3)E^{-8}$	$2.2E^{-4}$	$2.4E^{-4}$
H (1, 3)	$2.305066(3)E^{-7}$	$1.4E^{-6}$	$2.305022(4)E^{-7}$	$1.8E^{-6}$	$2.30512816232(1)E^{-7}$	$2.7E^{-5}$	$4.6E^{-5}$
He (2, 3)	$-1.3170511(4)E^{-6}$	$3E^{-7}$	$-1.3170088(3)E^{-6}$	$2E^{-7}$	$-1.317031330040(2)E^{-6}$	$-1.5E^{-5}$	$1.7E^{-5}$
K(19, 39)	$1.416801(3)E^{-4}$	$2E^{-6}$	$1.415971(3)E^{-4}$	$1.8E^{-6}$			
K(19, 40)	$-3.9639(8)E^{-4}$	$1.9E^{-4}$	$-3.9616(8)E^{-4}$	$1.9E^{-4}$			
K(19, 41)	$7.77649(4)E^{-5}$	$5E^{-6}$	$7.77191(3)E^{-5}$	$4E^{-6}$			
Rb(37, 85)	$3.50330(2)E^{-3}$	$7E^{-6}$	$3.497280(19)E^{-3}$	$5E^{-6}$			
Rb(37, 87)	$7.91520(4)E^{-3}$	$4E^{-6}$	$7.90160(3)E^{-3}$	$4E^{-6}$			
Cs(55, 133)	$2.38846(6)E^{-2}$	$2E^{-5}$	$2.37919(4)E^{-2}$	$1.8E^{-5}$			
Cs(55, 135)	$2.54604(19)E^{-2}$	$8E^{-5}$	$2.53615(19)E^{-2}$	$8E^{-5}$			
Pb (82, 207)	$4.5117(19)E^{-2}$	$4E^{-5}$	$4.46840(17)E^{-2}$	$4E^{-5}$	$4.4684(7)E^{-2}$	$-9.7E^{-3}$	$8.3E^{-3}$
Bi (83, 209)	$1.85493(12)E^{-1}$	$1.2E^{-5}$	$1.83335E^{-1}$	$1.0E^{-5}$	$1.86871(3)E^{-1}$	$1.4E^{-3}$	$3.5E^{-3}$
U(92, 235)	$-2.85(22)E^{-2}$	$8E^{-2}$	$-3.46(27)$	$8E^{-2}$			

We now compare our results for model (c) with experiment. Calculations for the ^{207}Pb ion yield:

$$\xi_c = 0.11105(8), \quad \eta_c = 0.02086(3).$$

Taking into account that $\Delta_0 = 5.1434(2) \times 10^{-2}$, we find

$$\Delta_c = 4.4858(2) \times 10^{-2},$$

hence

$$\tau_c = \frac{\Delta_{\text{exp}} - \Delta_c}{\Delta_{\text{exp}}} = -0.0039.$$

Comparing τ_c with $\tau_a = -0.0097$ and $\tau_b = 0.0083$ in Table XV, one can see that model (c) results are better for the ground-state hyperfine splitting than for models (a) and (b). However, $|\Delta_{\text{exp}} - \Delta_c| > \delta\Delta_c$.

Calculations for ^{209}Bi ion give:

$$\xi_c = 0.104649(27), \quad \eta_c = 0.020142(10).$$

Taking into account that $\Delta_0 = 2.14590(10)E^{-2}$, we get

$$\Delta_c = 0.185665(15)E^{-2},$$

such that

$$\tau_c = \frac{\Delta_{\text{exp}} - \Delta_c}{\Delta_{\text{exp}}} = 0.0064526.$$

Comparing τ_c with $\tau_a = 0.0014$ and $\tau_b = 0.0035$ in Table XV, one sees that model (a) gives somewhat better results for the ground-state hyperfine splitting than models (b) and (c) for ^{209}Bi .

IX. SUMMARY AND CONCLUSIONS

We calculated FNS corrections for the ground state ($1s$) and the first excited state ($2s$) of H&HLI using the Dirac equation with three different models for the atomic nucleus charge distribution. For model (a) [nuclear charge on the surface of the nucleus], we present the analytic solution of the Dirac equation, whereas for model (b) [nuclear charge uniformly distributed inside the nucleus] and model (c) [the two-parameter Fermi model – TPFM], we use both numerical calculations and first-order perturbation theory (the latter is not valid for large Z nuclei). The FNS corrections to the ground state energy and the first excited state energy are smaller than the electron-nucleus reduced mass correction and the relativistic QED radiative corrections for *light nuclei* (i.e., low Z nuclei) [33]. Nevertheless, it is important to obtain accurate FNS corrections so that a good comparison can be made with the extremely high-accuracy experimental results for hydrogen [18, 19] and deuterium [69, 70]. A detailed study of the hydrogen $1s$ - $2s$ transition has been reported in Ref. [28]. For heavy nuclei, the electron-nucleus reduced mass correction is small because $m_e/M(Z, A)$ is small, hence the FNS correction is larger than the electron-nucleus reduced mass correction. Furthermore, for heavy nuclei, $Z\alpha$ is not a small parameter, hence higher order relativistic QED radiative corrections, which can be neglected for hydrogen and light nuclei, are required, and therefore it is not clear whether FNS corrections are more important than relativistic QED radiative corrections since the latter have not been calculated.

We find that for H atoms and light HLI, the difference of the FNS corrections obtained using model (a)

and model (b), $\varepsilon_{n,a} - \varepsilon_{n,b}$, are small; the difference between model (a) and model (b) energies ε_n for $n = 1$ (the $1s$ state) and for $n = 2$ (the $2s$ state) is smaller than the uncertainties $\delta\varepsilon_{n,a}$ and $\delta\varepsilon_{n,b}$ in $\varepsilon_{n,a}$ and $\varepsilon_{n,b}$, see Tables III and IV. Hence, measurement of the $1s$ - $2s$ transition frequency cannot be used to determine details of the nuclear charge distribution for low Z nuclei [the perturbation theory expression in Eq. (69) is a good approximation for low Z nuclei, and perturbation theory expression does not depend on the details of the charge distribution, but only on r_N]. However, for heavy HLIs, the difference, $\varepsilon_{n,a} - \varepsilon_{n,b}$, is larger than the uncertainties $\delta\varepsilon_{n,a}$ and $\delta\varepsilon_{n,b}$ in $\varepsilon_{n,a}$ and $\varepsilon_{n,b}$. Thus measuring the $1s$ - $2s$ transition frequency for heavy nuclei HLIs can be used to determine not only the nuclear charge radii but the details of the nuclear charge distribution. Note that QED radiative corrections are available only for $Z\alpha \ll 1$. Hence, there is a problem applying the QED corrections for heavy nuclei.

Experimental results for the $1s$ - $3s$ transition frequency for hydrogen and deuterium have also been reported, see e.g., Ref. [65]. We intend to calculate this transition frequency to compare with these experiments in future work.

We have also calculated the FNS corrections for the ground-state *hyperfine splitting* of H&HLI using models (a), (b) and (c). After calculating the hyperfine splitting for point-like nuclei (model $\nu = 0$), we calculate the corrections ξ_ν (where $\nu = a, b, c$) due to the nuclear charge distribution, and the corrections η_ν due to the magnetic moment distribution. The percent uncertainties τ_ν of the theoretical results are compared with the experimental values [see Eq. (124)]. Both $|\tau_a|$ and $|\tau_b|$ are smaller than the correction ξ_ν to the hyperfine splitting. For ^1H atoms and ^3He ions, $|\tau_\nu| < \eta_\nu$. For ^2H , ^3H atoms, and ^{207}Pb and ^{209}Bi HLIs, $|\tau_\nu| > \eta_\nu$. We calculate also the ground-state hyperfine splitting for ^{207}Pb and ^{209}Bi HLIs with model (c) for the nuclear charge and magnetic moment distribution. For the ^{207}Pb HLI, model (c) gives a somewhat better result for the ground-state hyperfine splitting than models (a) and (b). For the ^{209}Bi HLI, model (a) gives a somewhat better result for the ground-state hyperfine splitting than models (b) and (c).

We show that $\xi_a > \eta_a$ for all the isotopes (see tables XII and XIII), i.e., the nuclear charge distribution correction to the ground-state hyperfine splitting is larger than the magnetic moment distribution correction. On the other hand, the difference $|\xi_a - \xi_b|$ is much larger than the uncertainties $\delta\xi_a$ and $\delta\xi_b$ in ξ_a and ξ_b , and the difference $|\eta_a - \eta_b|$ is much larger than the uncertainties $\delta\eta_a$ and $\delta\eta_b$ in η_a and η_b . Hence, it is crucial to test more accurate models of the nuclear charge and magnetic moment distributions in order to obtain results closer to experimental hyperfine splittings. The work that has been invested into calculating QED radiative corrections, can only bear fruit if accurate FNS corrections are developed. Given the fact that the FNS effects for hyperfine splittings are as big or bigger than the QED radiative corrections for all

the nuclei studied, how can one obtain more accurate nuclear charge and magnetic moment distributions in order to improve the FNS corrections? Several approaches are possible. (1) One can use more elaborate models for the charge and magnetic moment distributions. For example, one can use the three-parameter Fermi model, which has an additional term, $(1 + w_F r^2/c_F^2)$, multiplying the TPFM [24] or the double three-parameter Fermi model [63]. (2) Direct numerical fits to nuclear charge and magnetic moment distributions can be employed using data from electron scattering from nuclei [64]. (3) The charge and magnetic moment distributions are in general not equal, see e.g., Appendix D, hence distributions should be determined for each from experiment.

Acknowledgement: We would like to thank Shalom Shlomo for useful correspondence.

Appendix A: Nuclear charge radius

The nuclear charge radius $r_N = \sqrt{\langle r^2 \rangle_N}$ is defined as a RMS charge radius which is a measure of the normalized charge distribution $\rho_N(\mathbf{r})$,

$$\langle r^2 \rangle_N = \int r^2 \rho_N(r) d^3\mathbf{r}, \quad (\text{A1})$$

where $\rho_N(\mathbf{r})$ is normalized by the condition

$$\int \rho_N(\mathbf{r}) d^3\mathbf{r} = 1.$$

We now apply Eq. (A1) and calculate the nuclear radius for models (a) and (b).

Model (a): When the charge is distributed uniformly on a sphere of radius r_a , the normalized proton distribution $\rho_N(\mathbf{r}) \equiv \rho_a(r)$ is,

$$\rho_a(r) = \frac{Ze}{4\pi r_a^3} \delta(r - r_a), \quad (\text{A2})$$

Substituting Eq. (A2) into Eq. (A1), we get

$$r_a = r_N. \quad (\text{A3})$$

Model (b): When the charge is distributed uniformly inside a sphere of radius r_b , the normalized proton distribution $\rho_N(\mathbf{r}) \equiv \rho_b(r)$ is,

$$\rho_b(r) = \frac{3Ze}{4\pi r_b^3} \Theta(r_b - r), \quad (\text{A4})$$

where $\Theta(r_b - r)$ is equal to 1 for $r < r_b$, $\frac{1}{2}$ for $r = r_b$ and 0 for $r > r_b$. Substituting Eq. (A4) into Eq. (A1), we get $r_N = r_b \sqrt{3/5}$, or

$$r_b = r_N \sqrt{\frac{5}{3}}. \quad (\text{A5})$$

Appendix B: Matrix elements of $\mathbf{e}_r \times \boldsymbol{\alpha}$

The vector operator $\mathbf{e}_r \times \boldsymbol{\alpha}$ can be written as,

$$\mathbf{e}_r \times \boldsymbol{\alpha} = \begin{pmatrix} 0 & \mathbf{e}_r \times \boldsymbol{\sigma} \\ \mathbf{e}_r \times \boldsymbol{\sigma} & 0 \end{pmatrix},$$

where the 2×2 dimensional matrices $\mathbf{e}_r \times \boldsymbol{\sigma}$ are given by

$$\begin{aligned} \mathbf{e}_r \times \boldsymbol{\sigma} &= \begin{pmatrix} \sin \theta \sin \phi & i \cos \theta \\ -i \cos \theta & -\sin \theta \sin \phi \end{pmatrix} \mathbf{e}_x + \\ &\begin{pmatrix} -\sin \theta \cos \phi & \cos \theta \\ \cos \theta & \sin \theta \cos \phi \end{pmatrix} \mathbf{e}_y + \\ &\begin{pmatrix} 0 & -ie^{-i\phi} \\ ie^{i\phi} & 0 \end{pmatrix} \mathbf{e}_z. \end{aligned}$$

The matrix elements of $\mathbf{e}_r \times \boldsymbol{\alpha}$ with the wave functions $\psi_{m_J}(\mathbf{r})$ in Eq. (100) take the form,

$$\begin{aligned} &\int \psi_{m_J}^\dagger(\mathbf{r}) [\mathbf{e}_r \times \boldsymbol{\alpha}] \psi_{m'_J}(\mathbf{r}) \sin \theta d\theta d\phi \times \\ &= g(r)f(r) \int_0^\pi \sin \theta d\theta \int_0^{2\pi} d\phi \times \\ &\quad \left\{ i \Omega_{\frac{1}{2}0m_J}^\dagger [\mathbf{e}_r \times \boldsymbol{\sigma}] \Omega_{\frac{1}{2}1m'_J} + \text{c.c.} \right\} \\ &= -\frac{8}{3} g(r)f(r) \mathbf{J}_{m_J, m'_J}, \end{aligned} \quad (\text{B1})$$

where \mathbf{J}_{m_J, m'_J} are matrix elements of the orbital angular momentum operator \mathbf{J} .

Appendix C: Iteration method for determining s state energies using Eq. (58)

We shall now explain the iteration method, using the case of the ${}^3\text{He}$ ion for specificity. The ground-state energy of the ${}^3\text{He}$ ion for model (a) is $\varepsilon_1^{(0)} = 1.47460 \times 10^{-8} \epsilon_H$ (see Table III), where $\varepsilon_1^{(0)}$ is the ground-state energy of the He ion with the point-like nucleus given in Eq. (21). The energy using model (b) is close to the energy for model (a), see Table VIII below. Thus we take $\mathcal{E}_1 = \varepsilon_1^{(0)} - 4 \times 10^{-8} \epsilon_H$ as a first iteration for the energy. Solving Eq. (54) numerically for \mathcal{E} , we find $g_{b,-}(r), f_{b,-}(r)$ for $r < r_b$. Substituting $g_{b,-}(r_b), f_{b,-}(r_b)$, and $g_+(r_b), f_+(r_b)$ with \mathcal{E}_1 [see in Eq. (36)] into Eq. (58), we get $\mathcal{D}_1 \equiv \mathcal{D}(\mathcal{E}_1) = -5.16387 \times 10^{-5}$. The second iteration is $\mathcal{E}_2 = \varepsilon_1^{(0)} - 1.4 \times 10^{-8} \epsilon_H$. Solving Eq. (54) numerically for \mathcal{E}_2 , we find $g_{b,-}(r), f_{b,-}(r)$ for $r < r_b$. Substituting $g_{b,-}(r_b), f_{b,-}(r_b)$, and $g_+(r_b), f_+(r_b)$ with \mathcal{E}_2 [see in Eq. (36)] into Eq. (58), we get $\mathcal{D}_2 \equiv \mathcal{D}(\mathcal{E}_2) = 1.52535 \times 10^{-6}$. In order to find the third iteration for the ground-state energy ε , we plot a graph of $\mathcal{D}(\varepsilon)$ versus ε , with the two points, $(\mathcal{E}_1, \mathcal{D}_1)$, and $(\mathcal{E}_2, \mathcal{D}_2)$. We then connect these points by a line, and find the crossing point

\mathcal{E}_3 of this line with the x axis,

$$\mathcal{E}_3 = \frac{\mathcal{E}_1 \mathcal{D}_2 - \mathcal{E}_2 \mathcal{D}_1}{\mathcal{D}_2 - \mathcal{D}_1} = \varepsilon_1^{(0)} - 1.474597673 \times 10^{-8} \epsilon_H.$$

Solving Eq. (54) numerically for \mathcal{E}_3 , we find $g_{b,-}(r), f_{b,-}(r)$ for $r < r_b$. Substituting $g_{b,-}(r_b), f_{b,-}(r_b)$, and $g_+(r_b), f_+(r_b)$ with \mathcal{E}_3 [see in Eq. (36)] into Eq. (58), we get $\mathcal{D}_3 \equiv \mathcal{D}(\mathcal{E}_3) = 4.59235 \times 10^{-13}$. The fourth iteration for the energy is found from the equation,

$$\mathcal{E}_4 = \frac{\mathcal{E}_2 \mathcal{D}_3 - \mathcal{E}_3 \mathcal{D}_2}{\mathcal{D}_3 - \mathcal{D}_2} = \varepsilon_1^{(0)} - 1.474597699 \times 10^{-8} \epsilon_H,$$

such that $\mathcal{E}_3 - \mathcal{E}_4 = 2.6 \times 10^{-16} \epsilon_H$. Solving Eq. (54) numerically for \mathcal{E}_4 , we find $g_{b,-}(r), f_{b,-}(r)$ for $r < r_b$. Substituting $g_{b,-}(r_b), f_{b,-}(r_b)$, and $g_+(r_b), f_+(r_b)$ with \mathcal{E}_4 [see in Eq. (36)] into Eq. (58), we get $\mathcal{D}_4 \equiv \mathcal{D}(\mathcal{E}_4) = -9.41473 \times 10^{-13}$. Since $\mathcal{E}_3 - \mathcal{E}_4$ and \mathcal{D}_4 are very small, \mathcal{E}_4 is practically equal to the ${}^3\text{He}$ ground state energy.

Appendix D: Nuclear magnetic moment distribution for special nuclei

This appendix discusses the magnetic moment distribution for nuclei with one nucleon outside a closed nuclear shell.

1. Nuclear shell model

According to the nuclear shell model [59, 60], each nucleon in a nucleus moves in a self-consistent field due to the other nucleons. The nuclear self-consistent potential decreases rapidly outside the volume bounded by the surface of the nucleus. The quantum state of the nucleus is described by specifying the states of the individual nucleons. The self-consistent field is spherically symmetric, and the center of symmetry is the center of mass of the nucleus. Hence, the quantum states of the individual nucleons are parametrized by a radial quantum number n_r , angular momentum quantum number L , orbital angular momentum $J = L \pm 1/2$, and projection M_J of the vector $\mathbf{J} = \mathbf{L} + \mathbf{S}$. Nucleons fill shells according to the Pauli principle such that the nucleon states are distributed among the groups shown in Table XVI [59, 60]. For each group, the total number of proton or neutron occupation is shown. Hence, the occupation of a group is completed when the number Z of protons or the number N of neutrons is equal to one of the numbers: 2, 8, 28, 50, 82, 126, ... These numbers are called *magic numbers* [60]. Nuclei with both Z and N being magic numbers, are called *double magic* nuclei and have nuclear spin $I = 0$.

A nucleon moves in an effective attractive potential $V_{\text{nucl}}^{(j)}(r)$ formed by all the other nucleons. The potential $V_{\text{nucl}}^{(j)}(r)$ is given by [59]

$$V_{\text{nucl}}^{(j)}(r) = -\frac{V_j}{e^{(r-R_0)/a_F} + 1} + U_{\text{rep}}(r)\delta_{j,p}, \quad (\text{D1})$$

shells	nucleons
$1s_{1/2}$	2
$1p_{3/2}, 1p_{1/2}$	6
$1d_{5/2}, 2s_{1/2}, 1d_{3/2}, 1f_{7/2}$	20
$2p_{3/2}, 1f_{5/2}, 2p_{1/2}, 1g_{9/2}$	22
$2d_{5/2}, 1g_{7/2}, 1h_{11/2}, 2d_{3/2}, 3s_{1/2}$	32
$1h_{9/2}, 2f_{7/2}, 2i_{13/2}, 2f_{5/2}, 3p_{3/2}, 3p_{1/2}$	44

TABLE XVI. Groups of shells and the number of nucleon completing each group. Here the quantum number n_r before the letter is a radial quantum number, and the letters $s, p, d, f, g, h, i, \dots$ refer to the angular momentum quantum number, $L_j = 0, 1, 2, 3, 4, 5, 6, \dots$, where $j = p, n$ for protons and neutrons, and the subscript on the letters indicates the total orbital angular momentum of the nucleon, $J_j = L_j \pm 1/2$.

where the first term on the right hand side of Eq. (D1) is the Woods-Saxon attractive potential, and the second term, $U_{\text{rep}}(r)$, is the electrostatic repulsive interaction of a proton with the other $Z - 1$ protons in the nucleus. The Kronecker delta indicates that the Coulomb interaction is present for protons and absent for neutrons. Here $R_0 = 1.25 A^{1/3}$, and V_j is the depth of the potential well for protons ($j = p$) and neutrons ($j = n$). Note that $R_0 > c_F$, where c_F is the half-density nuclear radius in the two-parameter Fermi nuclear charge distribution, Eq. (80), and the difference $R_0 - c_F$ is due to the finite range of the nuclear force. The potential depth V_j is

$$V_j = U_0 + \eta_j U_1 \frac{N - Z}{A}, \quad (\text{D2})$$

where $U_0 = 57$ MeV, $U_1 = 27$ MeV, Z is the number of protons in the nucleus, N is the number of neutrons in the nucleus, and $A = Z + N$ is the total number of nucleons in the nucleus. The second term in the right hand side of Eq. (D2) is the symmetry energy arising when $Z \neq N$, where $\eta_p = 1$ and $\eta_n = -1$ [59]. The second term in the right hand side of Eq. (D1), $U_{\text{rep}}(r)$, is the electrostatic repulsion of a proton with the other $Z - 1$ protons in the nucleus. For the model (b) for the charge distribution, $U_{\text{rep}}(r)$ is

$$U_{\text{rep}}(r) = \begin{cases} \frac{(Z - 1)e^2}{2r_b} \left(3 - \frac{r^2}{r_b^2} \right), & \text{for } r \leq r_b, \\ \frac{(Z - 1)e^2}{r}, & \text{for } r > r_b. \end{cases}$$

In addition, spin-orbit interaction of a nucleon in the self-consistent potential is present, which is weaker than the strong interaction and can be taken into account using perturbation theory.

A nucleon wave function $\Psi_{n_r, L_j, M_L}(\mathbf{r})$ in a shell with the radial quantum number n_r , the angular momentum quantum number L_j and the projection M_L of the angular momentum \mathbf{L}_j on the z axis is found from the Schrödinger equation,

$$\left[-\frac{\hbar^2}{2M_j} \nabla^2 + V_{\text{nucl}}^{(j)}(r) \right] \Psi_{n_r, L_j, M_L}(\mathbf{r}) = \epsilon \Psi_{n_r, L_j, M_L}(\mathbf{r}), \quad (\text{D3})$$

where M_j is the nucleon mass. $\Psi_{n_r, L_j, M_L}(\mathbf{r})$ can be written as,

$$\Psi_{n_r, L_j, M_L}(\mathbf{r}) = \psi_{n_r, L_j}(r) Y_{L_j, M_L}(\theta, \phi),$$

where $\psi_{n_r, L_j}(r)$ is a radial wave function and $Y_{L_j, M_L}(\theta, \phi)$ is a spherical harmonic. $\psi_{n_r, L_j}(r)$ is found from the equation,

$$-\frac{\hbar^2}{2M_j r^2} \frac{d}{dr} \left(r^2 \frac{d\psi_{n_r, L_j}(r)}{dr} \right) + \frac{\hbar^2 L_j(L_j + 1)}{2M_j r^2} \psi_{n_r, L_j}(r) + V_{\text{nucl}}^{(j)}(r) \psi_{n_r, L_j}(r) = \epsilon \psi_{n_r, L_j}(r), \quad (\text{D4})$$

where the potential $V_{\text{nucl}}^{(j)}(r)$ is given in Eq. (D1).

We shall now apply the shell model to describe the nuclear magnetic moment distribution for ^{207}Pb and ^{209}Bi isotopes. For ^{207}Pb , $R_0 = 7.394$ fm, $c_F = 6.591$ fm, and the difference is $R_0 - c_F = 0.803$ fm. For ^{209}Bi , $R_0 = 7.418$ fm, $c_F = 6.765$ fm, and the difference is $R_0 - c_F = 0.653$ fm.

2. ^{207}Pb isotope nuclear density

The nucleus of ^{207}Pb consists of $Z = 82$ protons and $N = 125$ neutrons. Filling of the nuclear shells by the nucleons is illustrated in Fig. 11(a)(a): The number of protons is a magic number, i.e., the proton close the lowest shells and form a singlet state. The number of neutrons is one less than the magic number 126. The lowest 5 shells are closed by the neutrons, and the outer shell is partially filled with 43 neutrons. We consider the outer shell as a closed shell, partially filled by 1 hole, and derive the wave function for this hole. The nuclear spin I is equal to the orbital angular momentum of the hole. The nuclear spin of ^{207}Pb nucleus is $I = 1/2$. The hole is on the $3p_{1/2}$ orbit with the radial quantum number $n_r = 3$, angular momentum quantum number $L = 1$, and the orbital angular momentum quantum number $I = 1/2$.

Wave function $\Psi_{3,1,M_L}(\mathbf{r})$ of a hole with the radial quantum number $n_r = 3$, angular momentum number $L = 1$ and the projection M_L of \mathbf{L} on the z axis can be written as,

$$\Psi_{3,1,M_L}(\mathbf{r}) = \psi_{n_r, L}(r) Y_{L, M_L}(\theta, \phi),$$

where $\psi_{n_r, L}(r)$ is a radial wave function and $Y_{L, M_L}(\theta, \phi)$ is a spherical harmonics. $\psi_{n_r, L}(r)$ is found from the equation,

$$-\frac{\hbar^2}{2M_n r^2} \frac{d}{dr} \left(r^2 \frac{d\psi_{n_r, L}(r)}{dr} \right) + \frac{\hbar^2 L(L + 1)}{2M_n r^2} \psi_{n_r, L}(r) + V_{\text{nucl}}^{(n)}(r) \psi_{n_r, L}(r) = \epsilon \psi_{n_r, L}(r), \quad (\text{D5})$$

where M_n is the neutron mass, and the potential $V_{\text{nucl}}^{(n)}(r)$ is given in Eq. (D1) with $j = n$. We apply the *Mathematica* command NDEigensystem to solve Eq. (D4) and find

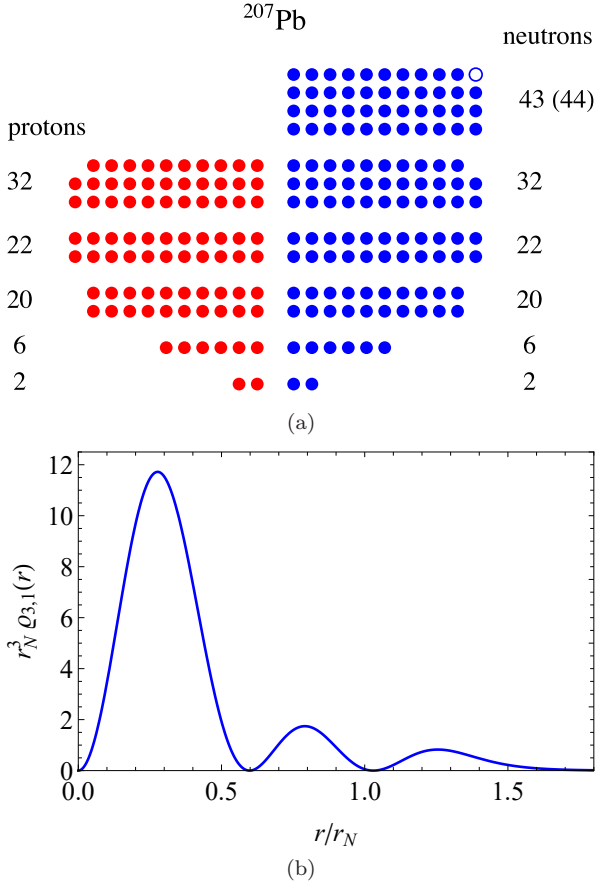


FIG. 11. (a) Protons (red) and neutrons (blue) in the ^{207}Pb nucleus fill the nuclear shells. The closed shells consist of 2, 6, 20, 22, 32 and 44 nucleons. The number of protons $Z = 82$ is a magic number, and the number of neutrons $N = 125$ is one less than the magic number 126. The empty circle shows the vacancy (a hole) in the outer shell. The nuclear spin $I = 1/2$ is the orbital angular momentum of the hole on the $3p_{1/2}$ shell. (b) Nuclear magnetic moment density for ^{207}Pb isotope.

radial wave functions $\psi_{n_r,1}(r)$ and energies of the $1p$, $2p$ and $3p$ states.

The magnetic moment density $\varrho_m(r)$ is

$$\varrho_m(r) = |\psi_{3,1}(r)|^2. \quad (\text{D6})$$

The magnetic moment density $\varrho_m(r)$ in Eq. (D6) is plotted in Fig. 11(b). $\varrho_m(r)$ has three nodes, at $r = 0$, $0.59821 r_N$ and $1.03036 r_N$, and three maxima, $\varrho_m(r_1) = 11.7192 r_N^{-3}$ at $r_1 = 0.277111 r_N$, $\varrho_m(r_2) = 1.74229 r_N^{-3}$ at $r_2 = 0.79112 r_N$, and $\varrho_m(r_3) = 0.824837 r_N^{-3}$ at $r_3 = 1.25533 r_N$. Note that the highest peak position r_1 in $\varrho(r)$ is far below r_N .

3. ^{209}Bi isotope nuclear density

The nucleus of ^{209}Bi consists of $Z = 83$ protons and $N = 126$ neutrons. Filling of the nuclear shells by the nucleons is illustrated in Fig. 12. The number of neutrons

is a magic number, i.e., the neutrons close the lowest 6 groups of shells and form a singlet state, see Table XVI. The number of protons is one more than the magic number 82. The lowest 5 groups of shells are closed by protons, and the outer shell is partially filled by a proton. The nuclear spin of ^{209}Bi , $I = 9/2$, is equal to the total orbital angular momentum $J_p = 9/2$ of the proton on the $1h_{9/2}$ shell with the radial quantum number $n_r = 1$, and the angular momentum quantum number $L_p = 5$.

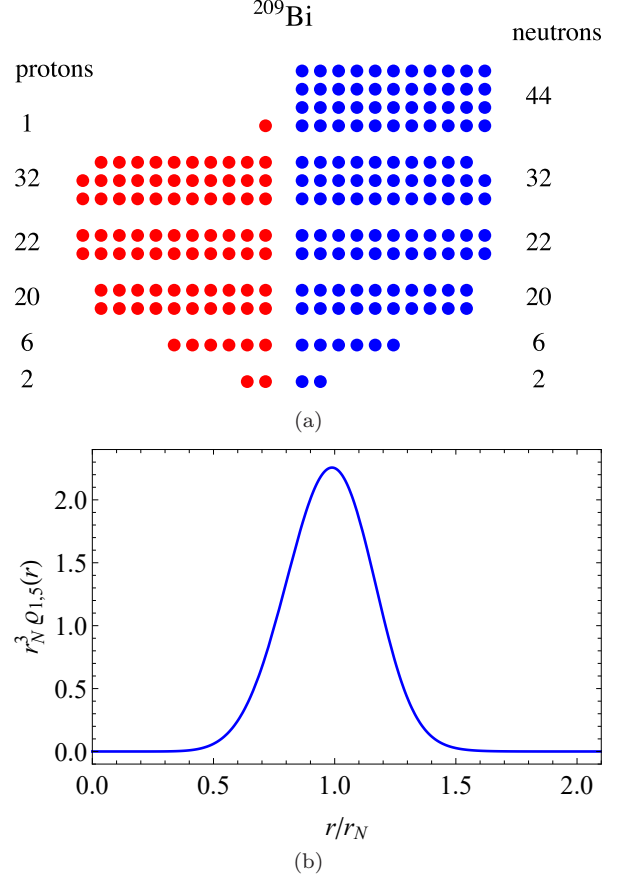


FIG. 12. (a) Protons (red) and neutrons (blue) in the ^{209}Bi nucleus fill the nuclear shells. The closed shells consist of 2, 6, 20, 22, 32, and 44 nucleons. The number of protons $Z = 83$ is one more than a magic number, and the number of neutrons $N = 126$ is a magic number. Nuclear spin $I = 9/2$ is equal to the orbital angular momentum of the proton occupying the outer $1h_{9/2}$ shell. (b) Nuclear magnetic moment density for ^{209}Bi isotope.

Using the *Mathematica* command `NDEigensystem`, we numerically solve Eq. (D4) to find the wave function $\psi_{1,5}(r)$ and the eigen-energy of the proton on the $1h$ shell.

The magnetic moment density $\varrho_m(r)$ of the ^{209}Bi nucleus is

$$\varrho_m(r) = |\psi_{1,5}(r)|^2. \quad (\text{D7})$$

The magnetic moment density $\varrho_m(r)$ in Eq. (D7) is plotted in Fig. 12(b). $\varrho_m(r)$ has a node at $r = 0$, increases with r , reaches its maximum, $\varrho_m(r_1) = 2.56639 r_N^{-3}$ at $r_1 = 0.988875 r_N$, decreases for $r > r_1$ and vanishing as

$r \rightarrow \infty$. The half-width of the peak at half-maximum is

$$\Delta R_0 = 0.211582 r_N, \text{ i.e., } \Delta R_0 \ll r_N.$$

-
- [1] H. A. Bethe and E. E. Salpeter, *Quantum Mechanics of One- And Two-Electron Atoms*, (Springer Verlag, Berlin, 1957).
- [2] A. I. Akhiezer, V.B. Berestetskii, *Quantum electrodynamics*, (John Wiley, NY, 1965).
- [3] J.J. Sakurai, *Advanced Quantum Mechanics*, (Addison-Wesley, Reading, MA, 1967).
- [4] V. B. Berestetskii, L. P. Pitaevskii, E.M. Lifshitz, *Quantum Electrodynamics: Volume 4 (Course of Theoretical Physics)*, 2nd Ed., (Butterworth-Heinemann, 1982).
- [5] J. Mawhin and A. Ronveaux, “Schrödinger and Dirac equations for the hydrogen atom, and Laguerre polynomials”, *Arch. Hist. Exact Sci.* **64**, 429 (2010).
- [6] L. Essen, M. J. Donaldson, M. J. Bangham, and E. G. Hope, *Nature* **229**, 110 (1971).
- [7] A. Dupays, A. Beswick, B. Lepetit, C. Rizzo, D. Bakalov, *Phys. Rev. A* **68**, 052503 (2003).
- [8] S. Kanda et al., *J. Phys.: Conf. Ser.* **1138**, 012009 (2018).
- [9] $1 \text{ Bohr} \equiv \frac{\hbar^2}{m_e e^2} = 5.2917721 \times 10^{-11} \text{ m} \equiv a_0$, this quantity is called the Bohr radius.
- [10] E. Tiesinga, P. J. Mohr, D. B. Newell, B. N. Taylor, *Rev. Mod. Phys.* **93**, 025010 (2021). This is the 2018 CODATA value of the proton root mean squared charge radius.
- [11] P. J. Mohr and B. N. Taylor, *Rev. Mod. Phys.* **77**, 1 (2005).
- [12] P. Beiersdorfer, S. B. Utter, K. L. Wong, J. R. C. Lopez-Urrutia, J. A. Britten, H. Chen, C. L. Harris, R. S. Thoe, D. B. Thorn, E. Trabert, M. G. H. Gustavsson, C. Forssen, and A.-M. Martensson-Pendrill, *Phys. Rev. A* **64**, 032506 (2001).
- [13] A. Bohr and V. F. Weisskopf, *Phys. Rev.* **77**, 94 (1950).
- [14] F.F. Karpeshin, M.B. Trzhaskovskaya, *Nuclear Physics A* **941**, 66 (2015).
- [15] A. Adamu, M. Hassan, M. K. Dikwa, S. A. Amshi, *American Journal of Quantum Chemistry and Molecular Spectroscopy* **2**, 39 (2018).
- [16] A.-M. Martensson-Pendrill and M.G.H. Gustavsson, “The Atomic Nucleus”, in *Handbook of Molecular Physics and Quantum Chemistry*, Vol. 1, pp. 477-484 (John Wiley & Sons, Ltd, Chichester, 2003).
- [17] R. T. Deck, J. G. Amar and G. Fralick, *J. Phys. B* **38**, 2173 (2005)
- [18] C. G. Parthey *et al.*, *Phys. Rev. Lett.* **107**, 203001 (2011).
- [19] A. Matveev *et al.*, *Phys. Rev. Lett.* **110**, 230801 (2013).
- [20] A. V. Volotka, D. A. Glazov, G. Plunien, and V. M. Shabaev, *Ann. Phys.* **525**, 636 (2013).
- [21] V.M. Shabaev, *J. Phys. B* **26**, 1103 (1993).
- [22] V. M. Shabaev, M. Tomaselli, T. Kühl, A. N. Artemyev, and V. A. Yerokhin, *Phys. Rev. A* **56**, 252 (1997).
- [23] I. A. Valuev, Z. Harman, C. H. Keitel, and N. S. Oreshkina “Skyrme-type nuclear interaction as a tool for calculating the finite-nuclear-size correction to atomic energy levels and the bound-electron g factor”, *Phys. Rev. A* **101**, 062502 (2020).
- [24] H. De Vries, C. W. De Jager, C. De Vries, *Atomic Data and Nuclear data Tables* **36**, 495536 (1987).
- [25] P. Sunnergren, H. Persson, S. Salomonson, S. M. Schneider, I. Lindgren, and G. Soff “Radiative corrections to the hyperfine-structure splitting of hydrogen-like systems” *Phys. Rev.* **58**, 1105 (1998)
- [26] A. V. Volotka, “High-precision QED calculations of the hyperfine structure in hydrogen and transition rates in multicharged ions”, Dissertation zur Erlangung des akademischen Grades Doctor rerum naturalium, Technische Universität Dresden, Dresden 2006.
- [27] I. Angeli and K. P. Marinova, *Atomic Data and Nuclear Data Tables* **99**, 69 (2013).
- [28] I. Kuzmenko, T. Kuzmenko, Y. Avishai, Y. B. Band, “Hydrogen 1s-2s transition frequency: Comparison of experiment and theory“, *Phys. Rev. Lett.* (submitted), arXiv:2211.05411.
- [29] V. B. Berestetskii, L. P. Pitaevskii, E.M. Lifshitz, *Relativistic quantum theory: Volume 4 part 1 (Course of Theoretical Physics)*, 2nd Ed., (Butterworth-Heinemann, 1971). *Ibid.* **4**, pp. 110-115.
- [30] K. Pachucki, D. Leibfried, M. Weitz, A. Huber, W. König and T. W. Hänsch, *J. Phys. B* **29**, 177 (1996).
- [31] N. Guang-Jiong, X. Jian-Jun, L. Sen-Yue, *Chin. Phys. B* **20**, 020302 (2011).
- [32] W. Greiner, *Relativistic Quantum Mechanics*, 3rd Ed., p. 250, Springer, Frankfurt am Main, 2000.
- [33] M. I. Eides, H. Grotch, and V. A. Shelyuto, *Theory of Light Hydrogenic Bound States*, (Springer-Verlag, Berlin, Heidelberg 2007).
- [34] <https://physics.nist.gov/cgi-bin/cuu/Info/Constants/definitions.html>. Briefly, if a measurement result $y = 1234.56789 \text{ U}$ and its uncertainty $u(y) = 0.00011 \text{ U}$, where U is the unit of y , then $Y = (1234.56789 \pm 0.00011) \text{ U}$. The concise form of this expression, and one that is in common use, is $Y = 1234.56789(11) \text{ U}$, where it understood that the number in parentheses is the numerical value of the uncertainty referred to the corresponding last digits of the quoted result.
- [35] *Ibid.* **4**, pp. 73-76.
- [36] P. J. Mohr, B. N. Taylor, D. B. Newell, *Rev. Mod. Phys.* **80**, 633 (2008).
- [37] T. J. Hänsch *et al.*, *Philos. Trans. R. Soc. London, Ser. A* **363**, 2155 (2005); T. W. Hänsch and H. Walther, *Rev. Mod. Phys.* **71**, S242 (1999).
- [38] T. Manovitz, R. Shaniv, Y. Shapira, R. Ozeri, N. Akerman, *Phys. Rev. Lett.* **123**, 203001 (2019).
- [39] https://en.wikipedia.org/wiki/Confluent_hypergeometric_function
- [40] The wave functions in Eqs. (36) and (45) are dimensionless and not normalized. The normalized wave function has additional factor \mathcal{N} given by Eq. (47). The dimensionality of \mathcal{N}_n is $[\mathcal{N}_n] = \text{cm}^{-3/2}$.
- [41] T. Hannesson and S. M. Blinder *Int. J. Quant. Chem.* **15**, 7 (1979).
- [42] Y. B. Band and Y. Avishai, *Quantum Mechanics, with Applications to Nanotechnology and Quantum Information Science*, (Academic Press – Elsevier, 2013), Sec. 4.6.
- [43] T. Hannesson and S. M. Blinder, *Int. J. Quantum Chem.* **15**, 7 (1979).
- [44] S. M. Blinder, *Theoret. Chim. Acta (Bed.)* **53**, 159

- (1979).
- [45] H. Hellwig, R. F. C. Vessot, M. V. Levine *et al.*, IEEE Trans. Instrum. Meas. **IM-19**, 200 (1970); L. Essen, M. J. Donaldson, M. J. Bangham, and E. G. Hope, Nature (London) **229**, 110 (1971).
- [46] “Nuclear isotope database”, <https://easyspin.org/documentation/isotopetable.html>.
- [47] *Handbook of Mathematical Functions*, edited by M. Abramowitz and I.A. Stegun (National Bureau of Standards, Washington, DC, 1964).
- [48] S. G. Karshenboim, Can. J. Phys. **78**, 639 (2000).
- [49] D. J. Wineland and N. F. Ramsey, Phys. Rev. **5**, 821 (1972).
- [50] B. S. Mathur *et al.*, Phys. Rev. **158**, 14 (1967).
- [51] H. A. Schluessler *et al.*, Phys. Rev. **187**, 5 (1969).
- [52] S. G. Karshenboim, and V. G. Ivanov, Phys.Rev. D **65**, 023510 (2002).
- [53] T. Stöhlker, “Precision Experiments in Atomic Physics with Heavy Ions”, http://pyweb.swan.ac.uk/quamp/quampweb/talks/13_09_11-QuAM02013-ThomasStoehlker.pdf.
- [54] J. Ullmann, Z. Andelkovic, C. Brandau, et al, Nature Communications **8**, 15484 (2017).
- [55] F. Biraben, Eur. Phys. J. Special Topics **172**, 109-119 (2009).
- [56] E. Arimondo, M. Inguscio, and P. Violino. Rev. Mod. Phys., **49**, 31 (1977).
- [57] P. Seelig, S. Borneis, A. Dax, T. Engel, S. Faber, M. Gerlach, C. Holbrow, G. Huber, T. Kühl, D. Marx, K. Meier, P. Merz, W. Quint, F. Schmitt, M. Tomaselli, L. Völker, H. Winter, M. Würtz, K. Beckert, B. Franzke, F. Nolden, H. Reich, M. Steck, and T. Winkler, Phys. Rev. Lett. **81**, 4824 (1998).
- [58] P. Raghavan, ADNDT **42**, 189 (1989).
- [59] “Shell Model of Nucleus”. HyperPhysics. <http://hyperphysics.phy-astr.gsu.edu/hbase/Nuclear/shell.html>
- [60] L. D. Landau and E. M. Lifshitz, Quantum Mechanics, Non-Relativistic Theory: Vol. 3 of Course of Theoretical Physics. [Pergamon press Ltd. 1965], pp. 447-456.
- [61] https://en.wikipedia.org/wiki/Isotopes_of_lead
- [62] https://en.wikipedia.org/wiki/Isotopes_of_bismuth
- [63] A. R. Abdulghany, Chinese Physics C **42**, 074101 (2018).
- [64] H. Überall, *Electron Scattering from Complex Nuclei*, (Academic Press, New York, 1971).
- [65] A. Grinin, *et al.*, Science **370**, 6520 (2020).
- [66] R. Pohl *et al.*, Nature **466**, 213?216 (2010).
- [67] A. Antognini *et al.*, Science **339**, 417?420 (2013).
- [68] A. Beyer, *et al.*, Science **358**, 79 (2017).
- [69] K. Pachucki, M. Weitz, and T. W. Hänsch, Phys. Rev. A **49**, 2255 (1994).
- [70] U. D. Jentschura, *et al.*, Phys. Rev. A **83**, 042505 (2011).